Cell

Article

Cell Membranes Resist Flow

Graphical Abstract

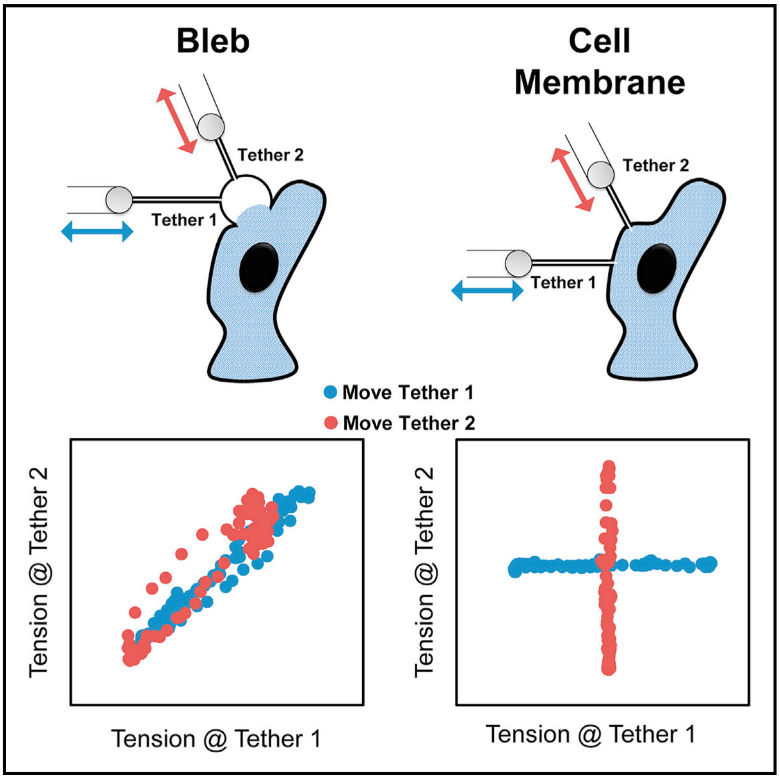

Highlights

- Cell membrane tension can vary substantially over micron-scale distances
- Transmembrane proteins bound to the cytoskeleton impede membrane flow
- Cell membrane tension propagates diffusively, as in a gel
- Localized changes in membrane tension lead to localized mechano-signaling

Authors

Zheng Shi, Zachary T. Graber,
Tobias Baumgart, Howard A. Stone,
Adam E. Cohen

Correspondence

cohen@chemistry.harvard.edu

In Brief

Changes in membrane tension do not spread over long distances in plasma membranes, which has implications for how mechanical stimuli are sensed and propagated in cells.

Shi et al., 2018, Cell *175*, 1–11
December 13, 2018 © 2018 Elsevier Inc.
https://doi.org/10.1016/j.cell.2018.09.054

CellPress

Please cite this article in press as: Shi et al., Cell Membranes Resist Flow, Cell (2018), https://doi.org/10.1016/j.cell.2018.09.054

Article

Cell

Cell Membranes Resist Flow

Zheng Shi,[1,4] Zachary T. Graber,[2] Tobias Baumgart,[2] Howard A. Stone,[3] and Adam E. Cohen[1,4,5,*]
[1]Department of Chemistry and Chemical Biology, Harvard University, Cambridge, MA 02138, USA
[2]Department of Chemistry, University of Pennsylvania, Philadelphia, PA 19104, USA
[3]Department of Mechanical and Aerospace Engineering, Princeton University, Princeton, NJ 08544, USA
[4]Howard Hughes Medical Institute
[5]Lead Contact
*Correspondence: cohen@chemistry.harvard.edu
https://doi.org/10.1016/j.cell.2018.09.054

SUMMARY

The fluid-mosaic model posits a liquid-like plasma membrane, which can flow in response to tension gradients. It is widely assumed that membrane flow transmits local changes in membrane tension across the cell in milliseconds, mediating long-range signaling. Here, we show that propagation of membrane tension occurs quickly in cell-attached blebs but is largely suppressed in intact cells. The failure of tension to propagate in cells is explained by a fluid dynamical model that incorporates the flow resistance from cytoskeleton-bound transmembrane proteins. Perturbations to tension propagate diffusively, with a diffusion coefficient D_σ ~0.024 μm^2/s in HeLa cells. In primary endothelial cells, local increases in membrane tension lead only to local activation of mechanosensitive ion channels and to local vesicle fusion. Thus, membrane tension is not a mediator of long-range intracellular signaling, but local variations in tension mediate distinct processes in sub-cellular domains.

INTRODUCTION

Membrane tension affects cell migration (Gauthier et al., 2011; Houk et al., 2012; Keren et al., 2008; Mueller et al., 2017), vesicle fusion and recycling (Boulant et al., 2011; Gauthier et al., 2011; Maritzen and Haucke, 2018; Masters et al., 2013; Shillcock and Lipowsky, 2005; Shin et al., 2018; Thottacherry et al., 2017; Wen et al., 2016), the cell cycle (Stewart et al., 2011), cell signaling (Basu et al., 2016; Groves and Kuriyan, 2010; Houk et al., 2012; Huse, 2017; Römer et al., 2007), and mechanosensation (He et al., 2018; Phillips et al., 2009; Ranade et al., 2015). However, there has been controversy over the speed and degree to which local changes in membrane tension propagate in cells (Diz-Muñoz et al., 2013). In artificial lipid bilayers, changes in membrane tension propagate across a cell-sized region in milliseconds (Figure S1; Shi and Baumgart, 2015). Fluorescently tagged transmembrane proteins typically diffuse freely in both artificial bilayers and in intact cells, albeit with a 10- to 100-fold lower diffusion coefficient in cells (Kusumi et al., 2005). Together, these results, each consistent with the fluid-mosaic model (Singer and Nicolson, 1972), led to the widespread belief that 2D flow of lipids in cells mediates rapid intracellular equilibration of membrane tension (Basu et al., 2016; Diz-Muñoz et al., 2013; Fogelson and Mogilner, 2014; Gauthier et al., 2011, 2012; Houk et al., 2012; Huse, 2017; Keren et al., 2008; Keren, 2011; Kozlov and Mogilner, 2007; Lieber et al., 2015; Morris and Homann, 2001; Mueller et al., 2017; Ofer et al., 2011; Pontes et al., 2017; Saha et al., 2018; Schweitzer et al., 2014; Sens and Plastino, 2015; Watanabe et al., 2013; Winkler et al., 2016), providing a long-range signaling mechanism analogous to the rapid propagation of electrical signals in neurons (Keren, 2011). Some studies have contemplated the possibility of tension gradients in rapidly migrating cells (Basu et al., 2016; Fogelson and Mogilner, 2014; Lieber et al., 2015; Schweitzer et al., 2014), but in these studies, the role of membrane-cytoskeleton friction was assumed to be a modest perturbation on the essentially fluid nature of the membrane.

Intact cell membranes contain many features not found in artificial lipid bilayers. In eukaryotic cells, approximately half of the transmembrane proteins, corresponding to ~10%–20% of total membrane area (Bussell et al., 1995; Zakharova et al., 1995), are bound to the underlying cortex and therefore are effectively immobile on timescales of minutes to hours (Bussell et al., 1995; Groves and Kuriyan, 2010; Sadegh et al., 2017). Are these obstacles a minor perturbation to lipid flow or do they qualitatively change the dynamics? Aqueous solutions with ~10% immobile protein, such as collagen gels, behave as bulk solids, not liquids, yet still permit lateral diffusion of small molecules and proteins. Thus, it is plausible that cell membranes too could exist in a state that behaves as a 2D fluid on the nanoscale but that is closer to a semi-solid gel on the cellular scale. The 2D-gel hypothesis is incompatible with the many conjectures in the literature that rapid propagation of membrane tension can mediate long-range intracellular signaling (Basu et al., 2016; Diz-Muñoz et al., 2013; Fogelson and Mogilner, 2014; Gauthier et al., 2011, 2012; Houk et al., 2012; Huse, 2017; Keren et al., 2008; Keren, 2011; Kozlov and Mogilner, 2007; Lieber et al., 2015; Morris and Homann, 2001; Mueller et al., 2017; Ofer et al., 2011; Pontes et al., 2017; Saha et al., 2018; Schweitzer et al., 2014; Sens and Plastino, 2015; Watanabe et al., 2013; Winkler et al., 2016).

RESULTS

Membrane Tension Propagates in Membrane Blebs, but Not in Cell Membranes

Working with HeLa cells at 37°C, we pulled short-membrane tethers as a means of simultaneously perturbing and measuring

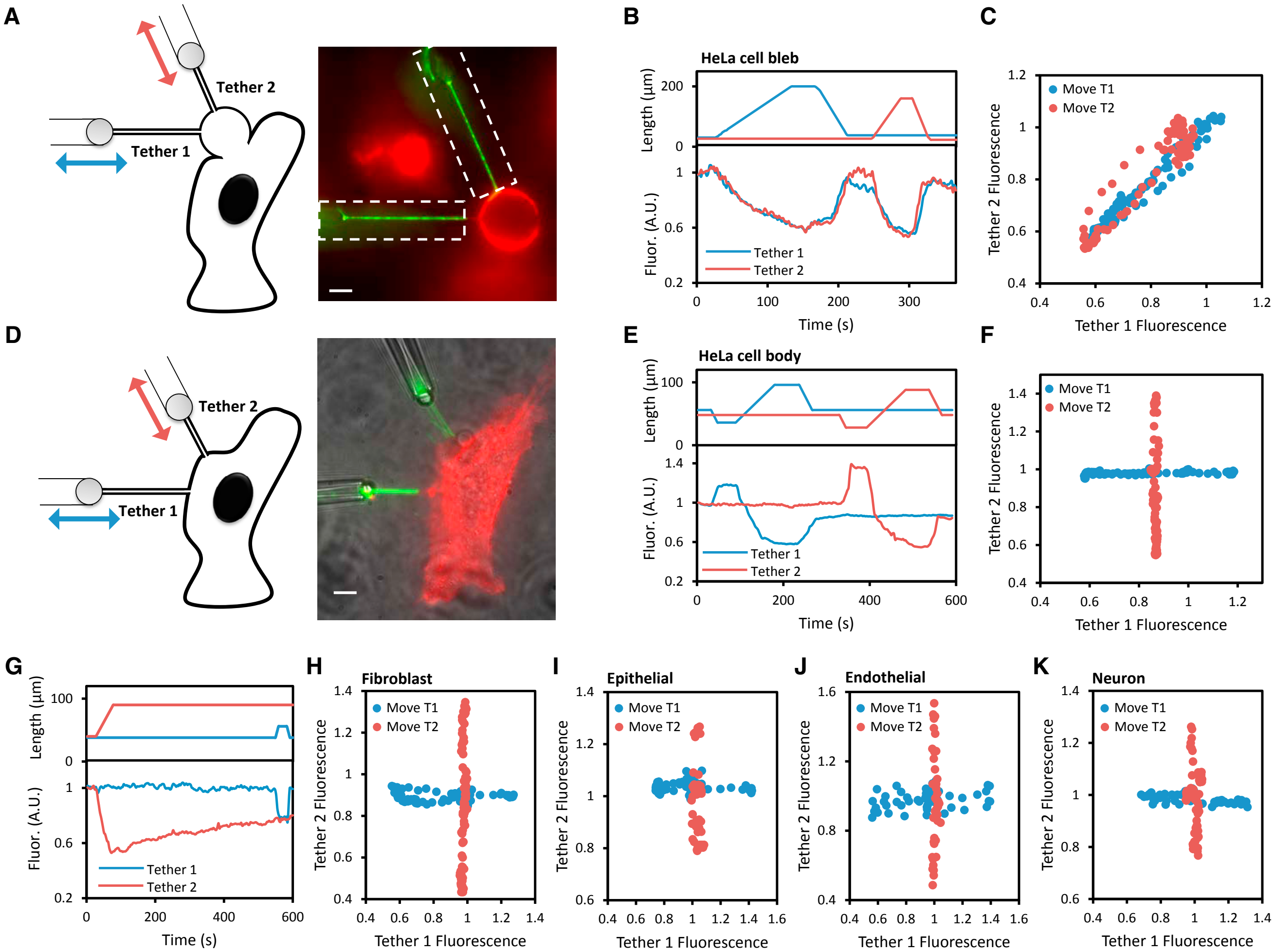

Figure 1. Propagation of Membrane Tension in Cells

(A and D) Schematic (left) and fluorescence image (right) showing a pair of tethers pulled from (A) a cell-attached bleb or (D) the cell body of a HeLa cell expressing GPI-eGFP. Green: fluorescence under patterned illumination (restricted to dashed boxes); red: fluorescence under wide-field illumination. In (D), a transmitted light image (gray) is combined with the fluorescence images. Scale bars 5 µm.

(B and E) The two tethers were stretched sequentially (top), and the fluorescence of each tether was monitored (bottom) in (B) a HeLa cell bleb and (E) an intact HeLa cell.

(C and F) Relation between the intensities of the two tethers when either the first or second tether was stretched in (C) a HeLa cell bleb and (F) an intact HeLa cell.

(G) Test for slow coupling between tethers in a HeLa cell. A change in length of tether 2 did not affect fluorescence of tether 1 within a 500-s measurement window.

(H–K) Repetition of the experiment in (D)–(F) in (H) NIH 3T3 fibroblasts, (I) MDCK epithelial cells, (J) mouse brain endothelial cells, and (K) rat hippocampal neurons. T1: tether 1; T2: tether 2.

See also Figures S1 and S2.

local membrane tension (Figures 1A and 1D). Tether diameter and local membrane tension are inversely related, coupled via the membrane's finite bending stiffness (Quantification and Statistical Analysis; Derényi et al., 2002; Pontes et al., 2017). Tether diameters were too small to resolve optically, so we used fluorescence of a membrane-bound tag (glycosylphosphatidylinositol-eGFP [GPI-eGFP]) to estimate tether diameter. Under wide-field fluorescence excitation, flare from the cell body prevented accurate quantification of the fluorescence from the far dimmer tether. We used a custom micromirror-based patterned illumination system to restrict fluorescence excitation to the tethers, leading to high-contrast images of individual tethers. By calibrating tether fluorescence against the fluorescence of a patch of cell membrane with known area, we determined the tether diameter. We used simultaneous fluorescence and optical trap force measurements to calibrate the relationship between tether diameter and tension (Figures S2A–S2D). Global perturbations to membrane tension via osmotic shocks induced the expected changes in both tether pulling force and tether fluorescence (Figures S2E–S2G).

Two membrane tethers were then simultaneously pulled from nearby locations on a single cell (typically 5–15 µm apart), and fluorescence from each was excited with micromirror-patterned illumination (Figures 1A, 1D, S2H, and S2I). Each tether was

Please cite this article in press as: Shi et al., Cell Membranes Resist Flow, Cell (2018), https://doi.org/10.1016/j.cell.2018.09.054

successively stretched and relaxed, and the fluorescence of both tethers was monitored to measure local tension. In cell-attached membrane blebs, we observed tight coupling of the tension in the two tethers (Figures 1A–1C). Stretching of either tether led to a decrease in the fluorescence of both tethers, with the response of the unstretched tether lagging by <1 s. Measurements on 10 pairs of tethers pulled from different blebs all showed strongly coupled fluorescence changes. Thus, tension rapidly equilibrated across blebs, consistent with observations in artificial lipid vesicles (e.g., Figure S1).

In intact cells, in contrast, we failed to observe any coupling between the tethers (Figures 1D–1F). Measurements lasted up to 500 s, and attachment points were as close as 5 μm (Figure 1G). We tested HeLa cells (Figures 1E and 1F; n = 30 cells), NIH 3T3 fibroblasts (Figure 1H; n = 10 cells), Madin-Darby canine kidney (MDCK) epithelial cells (Figure 1I; n = 5 cells), mouse brain endothelial cells (Figure 1J; n = 5 cells), and proximal dendrites of rat hippocampal neurons (Figure 1K; n = 5 neurons) and did not observe tension propagation in any of these cell types.

The failure to observe propagation of membrane tension in cells might be explained by rapid assembly of cytoskeletal barriers that isolated the tether from the rest of the cell. To test for such barriers, we first checked for the presence of actin in pulled tethers. In cells co-expressing a membrane label (mOrange2-KRAS) and an actin label (Lifeact-CFP), no actin signal was observed in the tether in experiments lasting up to 15 min (Figure S3A). We then performed fluorescence recovery after photobleaching (FRAP) experiments to test for diffusive interchange between the tether and the cell membrane. In cells expressing a transmembrane tracer, DRD2-eGFP, we photobleached all fluorescence in the tether and then monitored the recovery (Lippincott-Schwartz et al., 2003). The fluorescence recovery profile quantitatively matched simulations of free diffusion between the cell and tether, ruling out local cytoskeletal isolation of the tether (Figures S3B and S3C). Adhesive interactions between a tether and the cytoskeleton have been proposed to introduce an offset between the tether tension and the membrane tension (Dai and Sheetz, 1999), but such an offset would not affect the interpretation of our results.

Hydrodynamic Model of Membrane Flow

In two-dimensional flows, an immobile obstacle creates a logarithmically diverging long-range perturbation to the flow field, a phenomenon sometimes called the Stokes paradox. We hypothesized that cytoskeleton-bound transmembrane proteins might substantially impede the membrane flow required to propagate tension changes in cells (Figure 2A). Over length scales large compared to the inter-obstacle spacing, the poroelastic equations governing lipid flow lead to a diffusion-like equation for propagation of membrane tension, with tension diffusion coefficient $D_\sigma = E_m k/\eta$, where E_m is the effective area expansion modulus of the membrane, η is the two-dimensional membrane viscosity, and k is the Darcy permeability of the array of obstacles (Quantification and Statistical Analysis; see Table S1 for definitions and values for all physical parameters). The diffusion coefficient for the spread of membrane tension represents the balance of viscous and elastic forces in the membrane (Figure 2B) and is physically distinct from the diffusion coefficients that govern motion of tracer molecules within the lipid bilayer.

The Darcy permeability, k, scales with obstacle radius, a, and area fraction of the obstacles, Φ_i, as $k = a^2 f(\Phi_i)$, where $f(\Phi_i)$ is a dimensionless function that varies steeply at small Φ_i (Figure S3D; Bussell et al., 1995; Howells, 1974). Bussell et al. (1995) showed that one can estimate Φ_i from the diffusion of transmembrane tracer molecules. We compared the diffusion coefficients, D_S, of tracer molecules on an intact cell versus on cytoskeleton-free membrane tethers (Figures 2C, S3E, and S3F). For a transmembrane dopamine receptor fused to eGFP (DRD2-eGFP), FRAP measurements yielded diffusion coefficients on the cell 21 ± 4 fold lower than on the tether ($D_S^{\mathrm{cell}} = 0.037 \pm 0.005\ \mu m^2/s$; $D_S^{\mathrm{tether}} = 0.76 \pm 0.08\ \mu m^2/s$; mean ± SEM; n = 10 pairs of tethers and cells). We explored a variety of other tracers to control for possible molecularly specific interactions with cytoskeletal components and obtained similar results (Table S2), consistent with literature (Kusumi et al., 2005). We used the Saffman-Delbrück model (Saffman and Delbrück, 1975) to fit the diffusion on the cytoskeleton-free tethers and the Bussell model (Bussell et al., 1995) to fit the diffusion on the cell body. The pair of fits yielded a membrane viscosity $\eta = (3.0 \pm 0.4) \times 10^{-3}$ pN·s/μm and an area fraction of immobile obstacles $\Phi_i = 0.18 \pm 0.03$ (Figure 2C), consistent with literature results (Bussell et al., 1995; Kusumi et al., 2005).

We performed additional FRAP experiments to make an independent estimate of Φ_i in HeLa cells. Transmembrane proteins were labeled nonspecifically with a broadly reactive cell-impermeant dye and then photobleached in a sub-cellular region (Figure 2D). Mobile proteins thereafter diffused back into the bleached region, and immobile proteins did not. The degree of partial fluorescence recovery at long time (15 min) showed that 54% ± 5% (mean ± SEM; n = 5 cells) of all labeled transmembrane proteins were immobile (Figures 2E and S3G–S3I). When combined with literature estimates that ~25% of membrane area is occupied by transmembrane proteins (Dupuy and Engelman, 2008; Zakharova et al., 1995), these results are broadly consistent with our estimate of $\Phi_i = 0.1$–0.2 based on molecular diffusion measurements.

Combining the estimates of membrane viscosity, $\eta = (3.0 \pm 0.4) \times 10^{-3}$ pN·s/μm, and obstacle area fraction ($\Phi_i = 0.18 \pm 0.03$) with reasonable values of the obstacle radius ($a \sim 2$ nm; Bussell et al., 1995) and effective membrane area expansion modulus ($E_m = 40$ pN/μm; Hochmuth, 2000; Needham and Hochmuth, 1992) yields a tension diffusion coefficient: $D_\sigma = 0.024 \pm 0.005\ \mu m^2/s$. Tension therefore requires tens of minutes to equilibrate over cellular length scales (~10 μm). These experiments additionally yielded an estimate of an effective drag coefficient for membrane flow relative to the cytoskeleton, $\gamma = \eta/k$. We found $\gamma = 1{,}700 \pm 300$ pN·s/μm^3. Microrheometry measurement of cell plasma membrane with magnetic particles yielded a similar drag coefficient, $\gamma \approx 2{,}000$ pN·s/μm^3 (Bausch et al., 1998).

The hydrodynamic model establishes that the tension diffusion coefficient D_σ is far more sensitive to obstacles than is the tracer diffusion coefficient, D_S. An obstacle density that decreases tracer diffusion 10-fold from the free-membrane limit decreases diffusion of tension 10^4-fold (Figure 2C; Quantification and Statistical Analysis). Obstacles at densities that modestly suppress tracer diffusion will almost completely block lipid flow, causing the membrane to appear rheologically like a gel.

Please cite this article in press as: Shi et al., Cell Membranes Resist Flow, Cell (2018), https://doi.org/10.1016/j.cell.2018.09.054

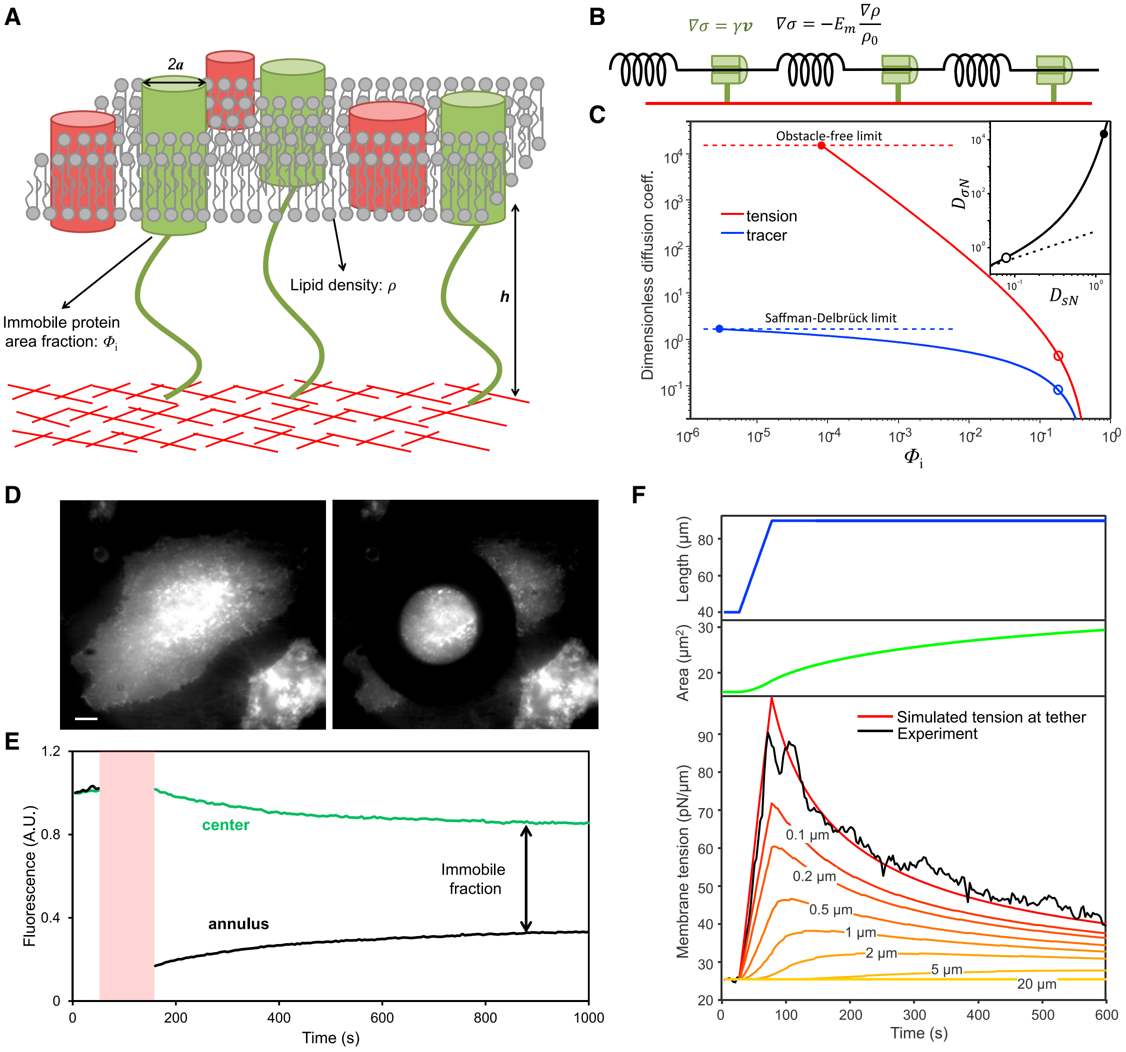

Figure 2. Hydrodynamic Model of Membrane Flow Past Immobile Obstacles

(A) Illustration of the cell plasma membrane with transmembrane proteins bound to the underlying cortex.

(B) Simple viscoelastic model of the cell membrane. Springs represent the elastic response of the membrane to stretch, and dampers represent the viscous drag from immobile transmembrane proteins.

(C) Dependence of diffusion coefficients for membrane tension (red) and molecular tracers (blue) on the area fraction Φ_i of immobile proteins. This plot shows the model's predictions for the dimensionless diffusion coefficients, $D_{\sigma N} = \eta D_\sigma / E_m a^2$ for tension and $D_{sN} = \pi \eta D_s / k_B T$ for tracers. The upper limit on tension diffusion is set by the hydrodynamic drag between plasma membrane and cytoskeleton cortex in the absence of obstacles. The upper limit on tracer diffusion is set by the Saffman-Delbrück model (Quantification and Statistical Analysis). Open circles: diffusion coefficients in intact cell membranes; inset: relation between dimensionless diffusion coefficients of membrane tension and molecular tracers (solid line). The dashed line shows a linear relation. Closed circles: obstacle-free membrane. Open circles: $\Phi_i = 0.18$.

(D) Fluorescence image showing a HeLa cell in which transmembrane proteins have been labeled non-specifically with Alexa488-NHS before (left) and after (right) bleaching with a donut shape laser spot. Scale bar, 10 μm.

(E) Fluorescence intensity profile of the bleached ring (black) and non-bleached central (green) regions. The photobleaching epoch is shaded red.

(F) Comparison of simulation and experiment for time-dependent membrane tension in a stretched membrane tether and surrounding cell membrane (E_m = 40 pN/μm; D_σ = 0.024 μm^2/s). (Top) Tether stretch protocol with initial tension σ_0 = 25 pN/μm and ramp increase in tether length from 40 μm to 90 μm at a pulling speed v_{pull} = 1 μm/s are shown. (Middle) Simulated surface area of the tether is shown. (Bottom) Membrane tension in the tether inferred from measurements of tether radius (black) and simulated membrane tension in the tether and in the cell at distances of 0.1 μm to 20 μm from the tether are shown. See Quantification and Statistical Analysis for details of the simulation.

See also Figure S3.

The hydrodynamic model predicts the distribution of membrane tension in space and time after a localized perturbation to the membrane. Using the experimentally determined tension diffusion coefficient (D_σ = 0.024 μm^2/s), we simulated the propagation of tension around a tether attachment point after a ramp increase in tether length. We accounted for the

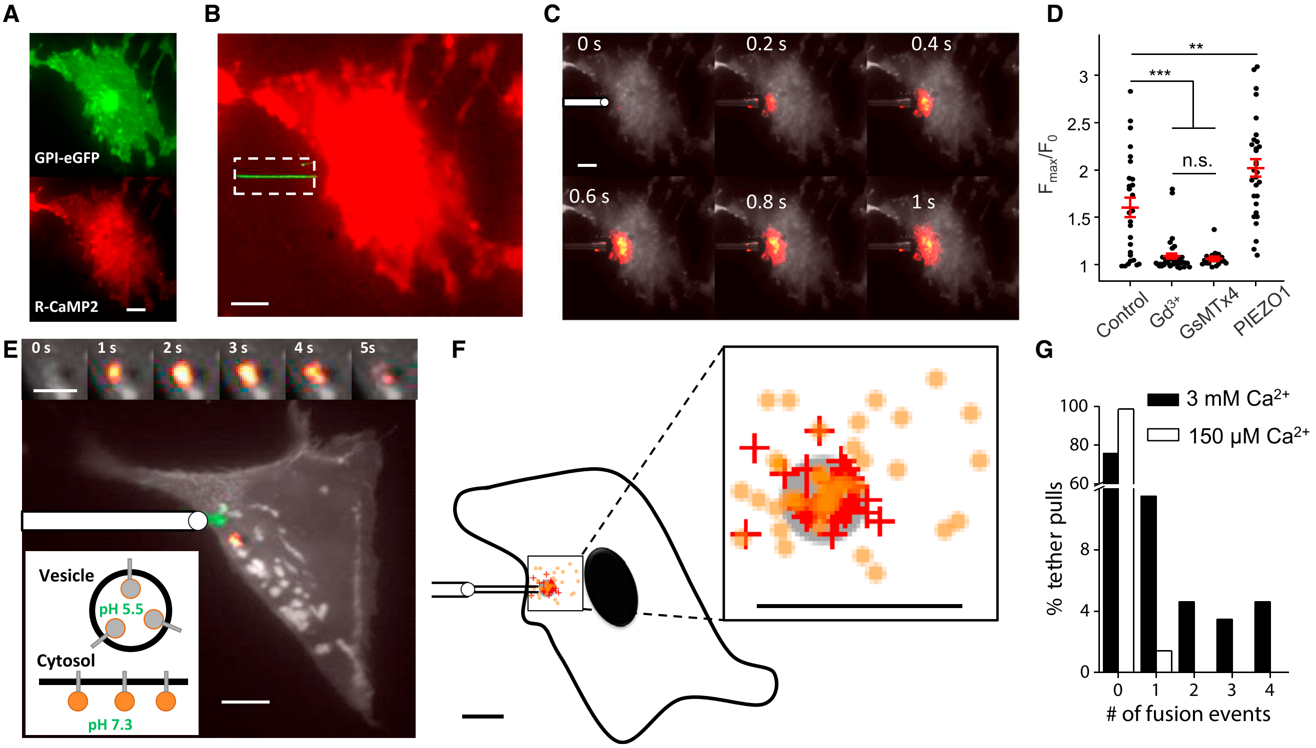

Figure 3. Membrane Tension Mediates Local Activation of Mechanosensitive Ion Channels and Local Vesicle Fusion in MDCK Cells

(A) MDCK cell co-expressing GPI-eGFP (green) and R-CaMP2 (red).

(B) Composite fluorescence image of tether (green) and R-CaMP2 (red). Fluorescence excitation of eGFP was confined to the tether (dashed box).

(C) Localized Ca^{2+} influx triggered by tether stretch. Images are composites of mean fluorescence (gray) and changes in fluorescence (heatmap). Tether pulling pipette shown schematically at 0 s.

(D) Blockers of MSCs, $GdCl_3$ (500 μM) or GsMTx4 (8 μM), suppressed Ca^{2+} influx during tether pulling. Overexpression of PIEZO1-mCherry increased Ca^{2+} influx during tether pulling (n = 27 cells in control extracellular buffer; n = 36 with $GdCl_3$; n = 18 with GsMTx4; n = 31 with PIEZO1 overexpression; $^{**}p < 0.01$; $^{***}p < 10^{-3}$, n.s.: $p > 0.5$; Student's t test). Data points represent maximal fractional increase in fluorescence of Ca^{2+} reporter. Red lines: mean. Error bars: SEM.

(E) Composite fluorescence image of mean fluorescence (gray), changes in fluorescence after tether pull (heatmap), and tether location (green). Tether pulling pipette shown schematically. (Upper inset) Close-up view of the vesicle fusion events triggered by tether stretch is shown. (Lower inset) Illustration of membrane-tethered mOrange2-TM as a reporter for vesicle fusion via pH-mediated changes in fluorescence is shown.

(F) Distribution of Ca^{2+} influx initiation points (+) and vesicle fusion (o) sites relative to the tether attachment point (gray circle). Each mark represents one event (33 Ca^{2+} influx events from 25 cells; 43 vesicle fusion events from 21 cells). Average distance between Ca^{2+} initiation and tether attachment was 1.7 ± 0.2 μm (mean ± SEM), smaller than the localization uncertainty (3 μm). Average distance between vesicle fusion site and tether attachment was 3.5 ± 0.4 μm (mean ± SEM), much smaller than the null hypothesis of uniform fusion throughout the cell (27 ± 2 μm). The outline of the cell is a schematic to illustrate size.

(G) In control extracellular medium (3 mM Ca^{2+}) tether pulling triggered fusion of one or more vesicles in 21 out of 87 trials (black). In low $[Ca^{2+}]$ buffer (150 μM Ca^{2+} buffered by EGTA) tether pulling triggered fusion of only one vesicle in 71 trials (white), establishing that elevated intracellular Ca^{2+} mediated vesicle fusion.

Scale bars in all panels 10 μm, except 5 μm for the upper inset in (E). See also Figures S4 and S5.

gradual changes in tether tension and radius as lipid flowed into the tether. These simulations, which had no adjustable parameters, quantitatively matched the measurements of the time-dependent tether tension (inferred from the tether radius; Figure 2F). The simulations predicted that the perturbation to membrane tension decayed to 50% of the maximum at 0.2 μm from the tether and to 3% of the maximum at 5 μm from the tether. Figure 2F shows that local perturbations to membrane tension remained predominantly localized within a sub-micron domain. For other perturbation geometries, the spatiotemporal distribution of membrane tension will depend on the geometry and time course of the perturbation and can be calculated by solving the diffusion equation.

Localized Activation of MSCs and Vesicle Fusion

To test whether membrane tension is a local or global regulator of membrane signaling, we examined the effect of local perturbations to tension on the activation of mechanosensitive ion channels (MSCs). We pulled tethers in endogenously mechanosensitive MDCK cells (Gudipaty et al., 2017) and performed simultaneous dual-color imaging of tether fluorescence (via GPI-eGFP) and intracellular Ca^{2+} (via R-CaMP2; Figures 3A–3C and S4A). These experiments revealed that MSCs in MDCK cells activated at a membrane tension ~10-fold higher than the resting tension (Figure S4D). We then switched to using GCaMP6f to improve Ca^{2+} sensitivity. In 18 out of 27 trials (15 out of 21 cells), tether pulling triggered Ca^{2+} influx (Figure 3D). In all tether-pulling experiments, the Ca^{2+} influx, if detected,

Please cite this article in press as: Shi et al., Cell Membranes Resist Flow, Cell (2018), https://doi.org/10.1016/j.cell.2018.09.054

initiated at the tether attachment to within our ability to resolve these two sites (Figure 3F). We never observed initiation of tether-induced Ca^{2+} influx in any regions of the cell distal from the tether attachment, even at the slowest pulling speeds tested (1 μm/s), establishing that membrane tension acted locally, not globally, to gate endogenous mechanosensitive ion channels. Ca^{2+} diffused from the point of entry to gradually fill the cell, consistent with the well-established role of Ca^{2+} as a mediator of long-range intracellular signaling.

The Ca^{2+} influx was largely blocked by Gd^{3+} (2 Ca^{2+} influx events in 36 tether pulls; Figure 3D), confirming that the influx was through stretch-activated mechanosensitive ion channels (Hua et al., 2010). The peptide toxin GsMTx4 also blocked the tether-induced Ca^{2+} influx (1 Ca^{2+} influx event in 18 tether pulls; Figure 3D). This toxin blocks PIEZO1, but not other MSCs, such as TREK-1 (Bae et al., 2011), suggesting that PIEZO1 likely mediates localized tension sensing in MDCK cells. Overexpression of PIEZO1-mCherry in MDCK cells led to increased but still localized Ca^{2+} influx during tether pulling (Figures 3D, S4E, and S4F), confirming that PIEZO1 responds to local, not global, membrane tension (Saotome et al., 2018). Sequential tether pulling from different locations of the same cell led to local Ca^{2+} influx at each pulling location, but not at the previously pulled site, further demonstrating sub-cellular compartmentalization of mechanosensation (Figure S4G).

Increases in membrane tension have been reported to facilitate vesicle release (Gauthier et al., 2011; Shillcock and Lipowsky, 2005; Shin et al., 2018). We next tested whether this effect was local or global. We expressed in MDCK cells membrane-tethered mOrange2 (mOrange2-TM), targeted to the inside of vesicles and to the extracellular face of the plasma membrane (Key Resources Table). This pH-sensitive reporter (pK_a 6.5; Shaner et al., 2008) was dark in the acidic lumen of vesicles and became fluorescent upon vesicle fusion to the plasma membrane (Figure 3E). Addition of the Ca^{2+} ionophore ionomycin (5 μM) led to Ca^{2+} influx and vesicle fusion as reported by the dye FM4-64, confirming that ionomycin triggered vesicle release (Figure S5). In MDCK cells expressing mOrange2-TM, ionomycin led to a cell-wide appearance of bright fluorescent puncta, confirming the ability of mOrange2-TM to report vesicle fusion (Figure S5). We then pulled tethers (from fresh cells expressing mOrange2-TM) and mapped the distribution of ensuing vesicle fusion events (Figures 3E and 3F). We compared to the distribution anticipated from the null hypothesis of uniform fusion throughout the cell (Method Details). The tension-induced events were significantly clustered around the tethers (Figure 3F; mean distance 3.5 ± 0.4 μm versus 27 ± 2 μm for null hypothesis; mean ± SEM; $n = 43$ fusion events from 21 cells).

The vesicle fusion events were more broadly distributed around the tether attachment points than were the Ca^{2+} influx initiation sites ($p = 0.001$), leading us to hypothesize that the vesicle fusion might be predominantly mediated by Ca^{2+} influx at the tether attachment and then Ca^{2+} diffusion over a larger but still sub-cellular region. Indeed, buffering extracellular Ca^{2+} concentration to 150 μM with EGTA largely eliminated tension-induced vesicle fusion (Figure 3G; only 1/71 pulls induced fusion), establishing that the local vesicle fusion was mediated by local influx of Ca^{2+} through MSCs followed by intracellular Ca^{2+} diffusion. Diffusion of Ca^{2+}, not propagation of membrane tension, caused the distribution of vesicle fusion events to extend beyond the tether attachment point.

Endothelial cells respond to changes in shear flow *in vivo* (Geiger et al., 1992; Li et al., 2014; Schwarz et al., 1992) via activation of PIEZO1 (Guo and MacKinnon, 2017). We thus asked whether tension-induced activation of mechanosensitive ion channels in primary mouse brain endothelial cells (mBECs) was local or global. As in the MDCK cells, tether pulling led to local influx of Ca^{2+} and local vesicle fusion (Figures 4A–4C and S4B). The vesicle fusion events were more broadly spread compared to in MDCK cells. We hypothesized that this effect was due to longer-range propagation of localized Ca^{2+} influx in mBEC cells due to Ca^{2+} induced endoplasmic reticulum (ER) Ca^{2+} release (Mumtaz et al., 2011). Pre-incubation of mBECs with 2-APB to deplete ER Ca^{2+} stores (Mumtaz et al., 2011) significantly reduced the spatial spread of tether-pulling-induced fusion events (Figure 4D). This result confirmed that, in mBECs, as in MDCK cells, intracellular spread of Ca^{2+}, not propagation of membrane tension, caused the distribution of vesicle fusion events to extend beyond the tether attachment point.

Tethers are a non-physiological perturbation, so we then tested the effect of localized shear flow on Ca^{2+} influx in mBECs. We used a small glass capillary (exit diameter 12 μm) to apply a sub-cellular flow to mBECs, with a maximal surface shear of 2×10^4 s^{-1}, corresponding to a surface stress of 20 pN/μm^2, approximately twice the mean value *in vivo* (Koller and Kaley, 1991). Bead tracers showed a nearly pencil-like laminar flow emerging from the pipette (Figure S6). This flow clearly induced localized Ca^{2+} influx (Figures 4E and S4C; $n = 5$ cells) and localized vesicle fusion (Figure 4F; $n = 4$ cells) in the high-shear zones, without activating either mechanosensitive channels or vesicle fusion in other parts of the cell. This experiment establishes that localized changes in membrane tension drive sub-cellular signaling in a physiologically relevant context.

DISCUSSION

Despite the well-established importance of membrane tension for many physiological processes (Basu et al., 2016; Boulant et al., 2011; Gauthier et al., 2011; Groves and Kuriyan, 2010; Houk et al., 2012; Huse, 2017; Keren et al., 2008; Maritzen and Haucke, 2018; Masters et al., 2013; Phillips et al., 2009; Ranade et al., 2015; Römer et al., 2007; Stewart et al., 2011), the path to equilibrium for local tension perturbations has not been measured quantitatively (Raucher and Sheetz, 1999). Most studies have assumed that membrane tension is homogeneous across a cell (Basu et al., 2016; Diz-Muñoz et al., 2013; Fogelson and Mogilner, 2014; Gauthier et al., 2011, 2012; Houk et al., 2012; Huse, 2017; Keren et al., 2008; Keren, 2011; Kozlov and Mogilner, 2007; Lieber et al., 2015; Morris and Homann, 2001; Mueller et al., 2017; Ofer et al., 2011; Pontes et al., 2017; Saha et al., 2018; Schweitzer et al., 2014; Sens and Plastino, 2015; Watanabe et al., 2013; Winkler et al., 2016). This assumption was justified either by analogy to isolated lipid bilayers (Keren et al., 2008; Watanabe et al., 2013) or by reference to experiments where membrane tension was globally perturbed via osmotic shocks or drug addition (Gauthier et al., 2011; Houk

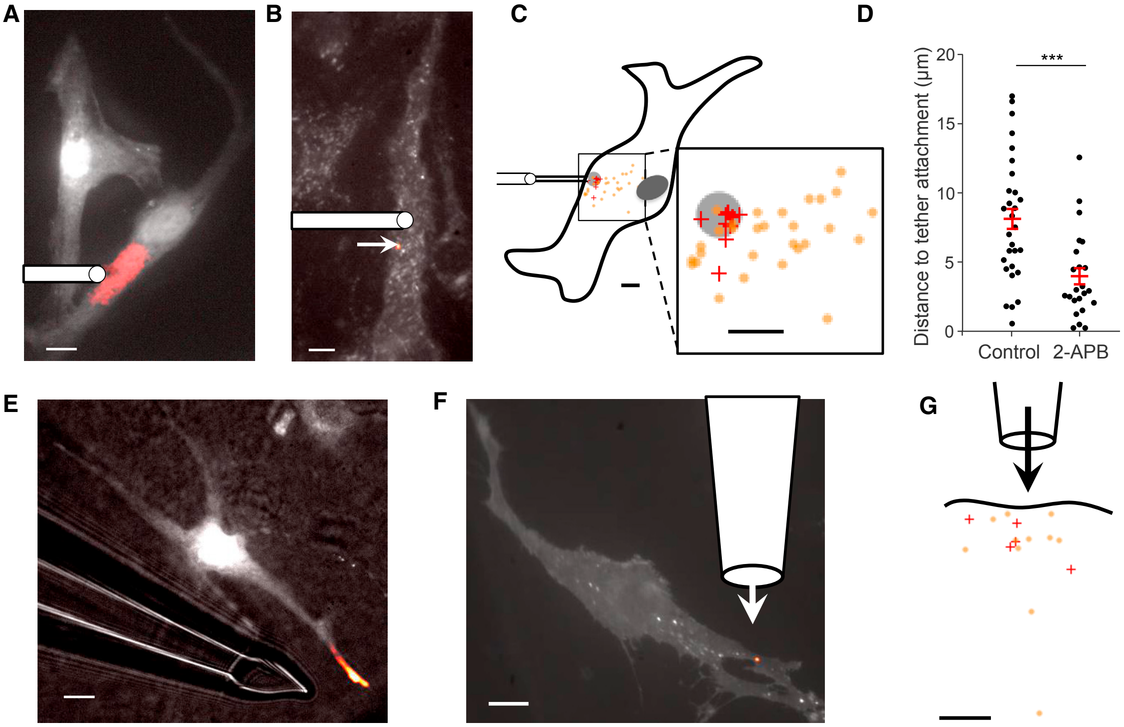

Figure 4. Tension Mediates Local Activation of Mechanosensitive Ion Channels and Local Vesicle Fusion in Primary Mouse Brain Endothelial Cells

(A and B) Tether stretch triggered (A) localized Ca^{2+} influx and (B) vesicle fusion events. Images are composites of mean fluorescence (gray) and changes in fluorescence (heatmap). Tether pulling pipette shown schematically.

(C) Distribution of Ca^{2+} influx (+) and vesicle fusion (o) sites relative to the tether attachment point (gray circle). Each mark represents one event (9 Ca^{2+} influx events from 7 cells; 29 vesicle fusion events from 6 cells). Average distance between Ca^{2+} initiation and tether attachment was 2.2 ± 0.5 μm (mean ± SEM), within the localization uncertainty (3 μm). Average distance between vesicle fusion and tether attachment was 8.0 ± 0.8 μm (mean ± SEM; versus 28 ± 3 μm for null hypothesis).

(D) 2-APB (100 μM) significantly reduced the spread of vesicle fusion events relative to the tether attachment (3.9 ± 0.6 μm; n = 23 with 2-APB; $^{***}p < 0.001$). Red lines: mean. Error bars: SEM.

(E and F) Local flow of extracellular buffer at 12 cm/s led to localized Ca^{2+} influx (E) and localized vesicle fusion (F). Images are composites of mean fluorescence (gray) and changes in fluorescence (heatmap). In (E), transmitted light shows the location of the pipette for flow delivery.

(G) Distribution of Ca^{2+} influx (+) and vesicle fusion (o) sites relative to the local flow. Each mark represents one flow-induced event (5 cells for Ca^{2+} influx; 11 fusion events from 4 cells for vesicle fusion).

Scale bars in all panels 10 μm. See also Figures S4 and S6.

et al., 2012; Mueller et al., 2017; Raucher and Sheetz, 2000). Several studies considered imbalances in membrane tension as a transient effect relevant to rapidly migrating cells (Basu et al., 2016; Fogelson and Mogilner, 2014; Lieber et al., 2015; Schweitzer et al., 2014).

Our data and model provide direct evidence that there is no long-range propagation of membrane tension in cells over ~10-min timescales. The diffusion coefficient for membrane tension, $D_\sigma \sim 0.024\ \mu m^2/s$, is so low that, on experimentally relevant timescales, imbalances in tension are essentially static. Local perturbations to tension can locally activate Ca^{2+} influx. Ca^{2+} ions diffuse in cytoplasm with a diffusion coefficient $D_{Ca} \sim 500\ \mu m^2/s$ (Donahue and Abercrombie, 1987) more than 20,000-fold higher than D_σ. Ca^{2+}-induced Ca^{2+} release can further enhance the propagation of local Ca^{2+} influx. Thus, Ca^{2+} provides a far more effective means of mediating long-range signaling than does membrane tension, and indeed, we observed Ca^{2+}-mediated vesicle release in regions distal to local mechanical perturbations (Figure 4C). Other small-molecule second messengers will also diffuse much faster than membrane tension.

The literature on activation of mechanosensitive ion channels in mammalian cells contains several inconsistencies. These inconsistencies are reconciled if one treats membrane tension as a local rather than a global parameter. For instance, activation of PIEZO1 mechanosensitive ion channels in cells via pipette aspiration produced a current proportional to the area of the pipette aperture, not the whole cell area (Cox et al., 2016; Gottlieb et al., 2012; Lewis and Grandl, 2015). This observation was reported as a surprise but is easily explained by the fact that the increased tension was localized near the pipette, not distributed over the cell.

In another example, direct measurements of resting cell membrane tension across various mammalian cells range from 3 to 40 pN/μm (Morris and Homann, 2001; Raucher and Sheetz, 1999), whereas the activation of mechanosensitive ion channels, such as PIEZO and TREK channels, has been reported to require a >100-fold higher membrane tension: 1,000~5,000 pN/μm (Cox et al., 2016; Gauthier et al., 2012; Morris and Homann, 2001). It was unclear how these channels were ever activated under physiological conditions. Our study shows that large local deviations in membrane tension can readily arise in cells, suggesting that measurements of mean cell-wide membrane tension may not be relevant to mechanosensation. For instance, when a cell has localized attachments to its matrix via focal adhesions, body forces applied to the cell can propagate through the cytoskeleton to localize the membrane stress at the attachment points. Consistent with this model, Ellefsen et al. (2018) recently reported that traction forces at focal adhesion sites induce local Ca^{2+} influx through PIEZO1, a phenomenon that would be hard to explain if membrane tension were homogeneous over the cell. The typical spacing between focal adhesions (~5 μm; Kim and Wirtz, 2013) is larger than the distance over which local perturbations to membrane tension propagate (Figure 2F), so gating of mechanosensitive ion channels occurs independently at distinct focal adhesions.

A third consequence of our model is the extreme sensitivity of the tension diffusion coefficient D_σ to the area fraction of cytoskeleton-bound obstacles, Φ_i, at low Φ_i. The dramatic effect of ~10% immobile obstacles on membrane rheology might seem counterintuitive. However, a similar effect is familiar in everyday life. An aqueous 10% collagen gel behaves as a solid and can be eaten with a fork. The Stokes paradox applies in both cases because, in the 3D gel, the proteins assemble into long 1D fibers, leading to an effectively 2D flow profile transverse to the fibers (Ramanujan et al., 2002). Although the density of transmembrane obstacles has not been systematically studied, we anticipate that this important biophysical parameter will vary between cell types, between sub-cellular regions, and throughout the cell cycle. There may be physiologically or pathophysiologically important situations (such as during mitosis or when cells are forming blebs) where tension can diffuse rapidly.

Changes in intracellular pressure could mediate long-range changes in membrane tension via the Laplace relation between pressure, membrane tension, and membrane curvature. A poroelastic model, analogous to our model for membrane tension, showed that intracellular hydrostatic pressure propagates diffusively, with a diffusion coefficient of D_P ~10 $\mu m^2/s$ (Charras et al., 2005). The more than 100-fold difference between D_P and D_σ reflects the correspondingly lower viscosity of cytosol versus membrane (Kusumi et al., 2005).

Cytoskeletal reorganization could also mediate long-range mechanical signaling (Bussonnier et al., 2014; Wu et al., 2013). One should think of the membrane and cytoskeleton as a composite material, in which deformation of the two components is tightly coupled. The far greater stiffness of the cytoskeleton compared to the membrane implies that the cytoskeleton dominates the rheology. In this composite picture, perturbations to the cytoskeleton could propagate quickly and cause long-range changes in membrane tension.

Several papers have proposed rapid transmission of membrane tension as a mechanism for long-range coordination of actin polymerization (Gauthier et al., 2011; Houk et al., 2012; Keren et al., 2008; Mueller et al., 2017). However, the membrane tension itself was not directly measured. Alternate mechanisms for long-range mechanical signaling include via hydrostatic pressure in the cytoplasm or via the actin cortex. We suggest these possibilities as alternate hypotheses to explain the literature data.

Many revisions to the fluid-mosaic model have been proposed (Nicolson, 2014). Specialized structures, such as cytoskeletal corrals and lipid rafts, have been invoked to explain sub-cellular confinement in membranes (Kusumi et al., 2005). Indeed, such structures are necessary to account for diffusional confinement and for local variations in membrane composition. Our results establish that a random array of transmembrane obstacles is sufficient to qualitatively change the membrane rheology from fluid to gel-like dynamics without invoking any specialized structures. This mechanism of membrane gelation is unrelated to the lipid gel phases that arise at lower temperatures through phase transitions of the lipids themselves (Koynova and Caffrey, 1998). Within our model, the lipids remain liquid-like on the nanoscale, permitting free diffusion of molecular cargoes. Our model is entirely consistent with the thermodynamic data used to support the fluid-mosaic model (Nicolson, 2014; Singer and Nicolson, 1972) while adding a picture of the slow and heterogeneous approach to equilibrium.

STAR★METHODS

Detailed methods are provided in the online version of this paper and include the following:

- KEY RESOURCES TABLE
- CONTACT FOR REAGENT AND RESOURCE SHARING
- EXPERIMENTAL MODEL AND SUBJECT DETAILS
  - ○ Cell culture, transfection, and staining
- METHOD DETAILS
  - ○ Bleb formation
  - ○ Glass micropipette fabrication, tether pulling, and imaging
  - ○ Tether pulling and Ca^{2+} imaging
  - ○ Tether pulling and vesicle fusion
  - ○ Local flow experiments with mBEC cells
- QUANTIFICATION AND STATISTICAL ANALYSIS
  - ○ Tether imaging analysis
  - ○ Fluorescence recovery after photobleaching (FRAP) measurements of diffusion
  - ○ FRAP measurement of fraction of transmembrane proteins that are immobile
  - ○ Simulation of relaxation of membrane tension in a tether
  - ○ Relation between tether radius, pulling force, and membrane tension
  - ○ Hydrodynamics of lipid flow
  - ○ Calculation of drag due to a random array of fixed cylinders
  - ○ Equation of state of membranes

SUPPLEMENTAL INFORMATION

Supplemental Information includes six figures and two tables and can be found with this article online at https://doi.org/10.1016/j.cell.2018.09.054.

ACKNOWLEDGMENTS

We thank Shahinoor Begum and Melinda Lee for help with neuron culture. We thank Katherine Williams, He Tian, Peng Zou, Yoav Adam, Linlin Fan, Sami Farhi, and Veena Venkatachalam for help with molecular cloning and plasmid preparation. We thank Sean Buchanan from Lee Rubin's lab and Harry McNamara for providing primary mouse brain endothelial cells and giving advice on the culturing protocols. We thank Xiaowei Zhuang's lab for providing NIH 3T3 fibroblasts. We thank Guido Guidotti, Boris Martinac, Charles Cox, Allen Liu, and Comert Kural for helpful comments. This work was supported by the Gordon and Betty Moore Foundation and the Howard Hughes Medical Institute. Z.T.G. and T.B. were supported by NIH grant R01 GM 09755 and NIH grant U54CA193417. H.A.S. was supported by NSF grants CBET-1509347 and DMS 1614907.

AUTHOR CONTRIBUTIONS

Z.S. and A.E.C. conceived the research, designed the experiments, analyzed the data, and wrote the paper. Z.S. carried out the experiments. Z.T.G. carried out the experiment in Figures S2A–S2D. T.B. contributed to experimental design and data interpretation. H.A.S. guided the theoretical analysis.

DECLARATION OF INTERESTS

The authors declare no competing interests.

Received: December 22, 2017
Revised: July 16, 2018
Accepted: September 26, 2018
Published: November 1, 2018

REFERENCES

Bae, C., Sachs, F., and Gottlieb, P.A. (2011). The mechanosensitive ion channel Piezo1 is inhibited by the peptide GsMTx4. Biochemistry *50*, 6295–6300.

Basu, R., Whitlock, B.M., Husson, J., Le Floc'h, A., Jin, W., Oyler-Yaniv, A., Dotiwala, F., Giannone, G., Hivroz, C., Biais, N., et al. (2016). Cytotoxic T cells use mechanical force to potentiate target cell killing. Cell *165*, 100–110.

Bausch, A.R., Ziemann, F., Boulbitch, A.A., Jacobson, K., and Sackmann, E. (1998). Local measurements of viscoelastic parameters of adherent cell surfaces by magnetic bead microrheometry. Biophys. J. *75*, 2038–2049.

Boulant, S., Kural, C., Zeeh, J.C., Ubelmann, F., and Kirchhausen, T. (2011). Actin dynamics counteract membrane tension during clathrin-mediated endocytosis. Nat. Cell Biol. *13*, 1124–1131.

Brochard-Wyart, F., Borghi, N., Cuvelier, D., and Nassoy, P. (2006). Hydrodynamic narrowing of tubes extruded from cells. Proc. Natl. Acad. Sci. USA *103*, 7660–7663.

Bussell, S.J., Koch, D.L., and Hammer, D.A. (1995). Effect of hydrodynamic interactions on the diffusion of integral membrane proteins: diffusion in plasma membranes. Biophys. J. *68*, 1836–1849.

Bussonnier, M., Carvalho, K., Lemière, J., Joanny, J.F., Sykes, C., and Betz, T. (2014). Mechanical detection of a long-range actin network emanating from a biomimetic cortex. Biophys. J. *107*, 854–862.

Charras, G.T., Yarrow, J.C., Horton, M.A., Mahadevan, L., and Mitchison, T.J. (2005). Non-equilibration of hydrostatic pressure in blebbing cells. Nature *435*, 365–369.

Chen, T.W., Wardill, T.J., Sun, Y., Pulver, S.R., Renninger, S.L., Baohan, A., Schreiter, E.R., Kerr, R.A., Orger, M.B., Jayaraman, V., et al. (2013). Ultrasensitive fluorescent proteins for imaging neuronal activity. Nature *499*, 295–300.

Clausen, M.P., Colin-York, H., Schneider, F., Eggeling, C., and Fritzsche, M. (2017). Dissecting the actin cortex density and membrane-cortex distance in living cells by super-resolution microscopy. J. Phys. D Appl. Phys. *50*, 064002.

Cox, C.D., Bae, C., Ziegler, L., Hartley, S., Nikolova-Krstevski, V., Rohde, P.R., Ng, C.A., Sachs, F., Gottlieb, P.A., and Martinac, B. (2016). Removal of the mechanoprotective influence of the cytoskeleton reveals PIEZO1 is gated by bilayer tension. Nat. Commun. *7*, 10366.

Dai, J., and Sheetz, M.P. (1999). Membrane tether formation from blebbing cells. Biophys. J. *77*, 3363–3370.

Derényi, I., Jülicher, F., and Prost, J. (2002). Formation and interaction of membrane tubes. Phys. Rev. Lett. *88*, 238101.

Diz-Muñoz, A., Fletcher, D.A., and Weiner, O.D. (2013). Use the force: membrane tension as an organizer of cell shape and motility. Trends Cell Biol. *23*, 47–53.

Domanov, Y.A., Aimon, S., Toombes, G.E.S., Renner, M., Quemeneur, F., Triller, A., Turner, M.S., and Bassereau, P. (2011). Mobility in geometrically confined membranes. Proc. Natl. Acad. Sci. USA *108*, 12605–12610.

Donahue, B.S., and Abercrombie, R.F. (1987). Free diffusion coefficient of ionic calcium in cytoplasm. Cell Calcium *8*, 437–448.

Dupuy, A.D., and Engelman, D.M. (2008). Protein area occupancy at the center of the red blood cell membrane. Proc. Natl. Acad. Sci. USA *105*, 2848–2852.

Ellefsen, K., Chang, A., Nourse, J.L., Holt, J.R., Arulmoli, J., Mekhdjian, A., Flanagan, L.A., Dunn, A.R., Parker, I., and Pathak, M.M. (2018). Piezo1 calcium flickers localize to hotspots of cellular traction forces. bioRxiv. https://doi.org/10.1101/294611.

Evans, E., and Rawicz, W. (1990). Entropy-driven tension and bending elasticity in condensed-fluid membranes. Phys. Rev. Lett. *64*, 2094–2097.

Fogelson, B., and Mogilner, A. (2014). Computational estimates of membrane flow and tension gradient in motile cells. PLoS One *9*, e84524.

Gauthier, N.C., Rossier, O.M., Mathur, A., Hone, J.C., and Sheetz, M.P. (2009). Plasma membrane area increases with spread area by exocytosis of a GPI-anchored protein compartment. Mol. Biol. Cell *20*, 3261–3272.

Gauthier, N.C., Fardin, M.A., Roca-Cusachs, P., and Sheetz, M.P. (2011). Temporary increase in plasma membrane tension coordinates the activation of exocytosis and contraction during cell spreading. Proc. Natl. Acad. Sci. USA *108*, 14467–14472.

Gauthier, N.C., Masters, T.A., and Sheetz, M.P. (2012). Mechanical feedback between membrane tension and dynamics. Trends Cell Biol. *22*, 527–535.

Geiger, R.V., Berk, B.C., Alexander, R.W., and Nerem, R.M. (1992). Flow-induced calcium transients in single endothelial cells: spatial and temporal analysis. Am. J. Physiol. *262*, C1411–C1417.

Gottlieb, P.A., Bae, C., and Sachs, F. (2012). Gating the mechanical channel Piezo1: a comparison between whole-cell and patch recording. Channels (Austin) *6*, 282–289.

Groves, J.T., and Kuriyan, J. (2010). Molecular mechanisms in signal transduction at the membrane. Nat. Struct. Mol. Biol. *17*, 659–665.

Gudipaty, S.A., Lindblom, J., Loftus, P.D., Redd, M.J., Edes, K., Davey, C.F., Krishnegowda, V., and Rosenblatt, J. (2017). Mechanical stretch triggers rapid epithelial cell division through Piezo1. Nature *543*, 118–121.

Guo, Y.R., and MacKinnon, R. (2017). Structure-based membrane dome mechanism for Piezo mechanosensitivity. eLife *6*, e33660.

He, L., Tao, J., Maity, D., Si, F., Wu, Y., Wu, T., Prasath, V., Wirtz, D., and Sun, S.X. (2018). Role of membrane-tension gated Ca^{2+} flux in cell mechanosensation. J. Cell. Sci. *131*, jcs208470.

Heinrich, M., Tian, A., Esposito, C., and Baumgart, T. (2010). Dynamic sorting of lipids and proteins in membrane tubes with a moving phase boundary. Proc. Natl. Acad. Sci. USA *107*, 7208–7213.

Hochbaum, D.R., Zhao, Y., Farhi, S.L., Klapoetke, N., Werley, C.A., Kapoor, V., Zou, P., Kralj, J.M., Maclaurin, D., Smedemark-Margulies, N., et al. (2014). All-optical electrophysiology in mammalian neurons using engineered microbial rhodopsins. Nat. Methods *11*, 825–833.

Hochmuth, R.M. (2000). Micropipette aspiration of living cells. J. Biomech. *33*, 15–22.

Hochmuth, R.M., Mohandas, N., and Blackshear, P.L., Jr. (1973). Measurement of the elastic modulus for red cell membrane using a fluid mechanical technique. Biophys. J. *13*, 747–762.

Houk, A.R., Jilkine, A., Mejean, C.O., Boltyanskiy, R., Dufresne, E.R., Angenent, S.B., Altschuler, S.J., Wu, L.F., and Weiner, O.D. (2012). Membrane tension maintains cell polarity by confining signals to the leading edge during neutrophil migration. Cell *148*, 175–188.

Howells, I.D. (1974). Drag due to the motion of a Newtonian fluid through a sparse random array of small fixed rigid objects. J. Fluid Mech. *64*, 449–476.

Hua, S.Z., Gottlieb, P.A., Heo, J., and Sachs, F. (2010). A mechanosensitive ion channel regulating cell volume. Am. J. Physiol. Cell Physiol. *298*, C1424–C1430.

Huse, M. (2017). Mechanical forces in the immune system. Nat. Rev. Immunol. *17*, 679–690.

Inoue, M., Takeuchi, A., Horigane, S., Ohkura, M., Gengyo-Ando, K., Fujii, H., Kamijo, S., Takemoto-Kimura, S., Kano, M., Nakai, J., et al. (2015). Rational design of a high-affinity, fast, red calcium indicator R-CaMP2. Nat. Methods *12*, 64–70.

Jiang, M., and Chen, G. (2006). High Ca2+-phosphate transfection efficiency in low-density neuronal cultures. Nat. Protoc. *1*, 695–700.

Kang, M., Day, C.A., Kenworthy, A.K., and DiBenedetto, E. (2012). Simplified equation to extract diffusion coefficients from confocal FRAP data. Traffic *13*, 1589–1600.

Keren, K. (2011). Cell motility: the integrating role of the plasma membrane. Eur. Biophys. J. *40*, 1013–1027.

Keren, K., Pincus, Z., Allen, G.M., Barnhart, E.L., Marriott, G., Mogilner, A., and Theriot, J.A. (2008). Mechanism of shape determination in motile cells. Nature *453*, 475–480.

Kim, D.H., and Wirtz, D. (2013). Focal adhesion size uniquely predicts cell migration. FASEB J. *27*, 1351–1361.

Koller, A., and Kaley, G. (1991). Endothelial regulation of wall shear stress and blood flow in skeletal muscle microcirculation. Am. J. Physiol. *260*, H862–H868.

Koynova, R., and Caffrey, M. (1998). Phases and phase transitions of the phosphatidylcholines. Biochim. Biophys. Acta *1376*, 91–145.

Kozlov, M.M., and Mogilner, A. (2007). Model of polarization and bistability of cell fragments. Biophys. J. *93*, 3811–3819.

Kralj, J.M., Hochbaum, D.R., Douglass, A.D., and Cohen, A.E. (2011). Electrical spiking in Escherichia coli probed with a fluorescent voltage-indicating protein. Science *333*, 345–348.

Kusumi, A., Nakada, C., Ritchie, K., Murase, K., Suzuki, K., Murakoshi, H., Kasai, R.S., Kondo, J., and Fujiwara, T. (2005). Paradigm shift of the plasma membrane concept from the two-dimensional continuum fluid to the partitioned fluid: high-speed single-molecule tracking of membrane molecules. Annu. Rev. Biophys. Biomol. Struct. *34*, 351–378.

Lewis, A.H., and Grandl, J. (2015). Mechanical sensitivity of Piezo1 ion channels can be tuned by cellular membrane tension. eLife *4*, e12088.

Li, J., Hou, B., Tumova, S., Muraki, K., Bruns, A., Ludlow, M.J., Sedo, A., Hyman, A.J., McKeown, L., Young, R.S., et al. (2014). Piezo1 integration of vascular architecture with physiological force. Nature *515*, 279–282.

Lieber, A.D., Schweitzer, Y., Kozlov, M.M., and Keren, K. (2015). Front-to-rear membrane tension gradient in rapidly moving cells. Biophys. J. *108*, 1599–1603.

Lippincott-Schwartz, J., Altan-Bonnet, N., and Patterson, G.H. (2003). Photobleaching and photoactivation: following protein dynamics in living cells. Nat. Cell Biol., S7–S14.

Maritzen, T., and Haucke, V. (2018). Coupling of exocytosis and endocytosis at the presynaptic active zone. Neurosci. Res. *127*, 45–52.

Masters, T.A., Pontes, B., Viasnoff, V., Li, Y., and Gauthier, N.C. (2013). Plasma membrane tension orchestrates membrane trafficking, cytoskeletal remodeling, and biochemical signaling during phagocytosis. Proc. Natl. Acad. Sci. USA *110*, 11875–11880.

Morris, C.E., and Homann, U. (2001). Cell surface area regulation and membrane tension. J. Membr. Biol. *179*, 79–102.

Mueller, J., Szep, G., Nemethova, M., de Vries, I., Lieber, A.D., Winkler, C., Kruse, K., Small, J.V., Schmeiser, C., Keren, K., et al. (2017). Load adaptation of lamellipodial actin networks. Cell *171*, 188–200.e16.

Mumtaz, S., Burdyga, G., Borisova, L., Wray, S., and Burdyga, T. (2011). The mechanism of agonist induced Ca2+ signalling in intact endothelial cells studied confocally in in situ arteries. Cell Calcium *49*, 66–77.

Needham, D., and Hochmuth, R.M. (1992). A sensitive measure of surface stress in the resting neutrophil. Biophys. J. *61*, 1664–1670.

Nicolson, G.L. (2014). The fluid-mosaic model of membrane structure: still relevant to understanding the structure, function and dynamics of biological membranes after more than 40 years. Biochim. Biophys. Acta *1838*, 1451–1466.

Ofer, N., Mogilner, A., and Keren, K. (2011). Actin disassembly clock determines shape and speed of lamellipodial fragments. Proc. Natl. Acad. Sci. USA *108*, 20394–20399.

Phillips, R., Ursell, T., Wiggins, P., and Sens, P. (2009). Emerging roles for lipids in shaping membrane-protein function. Nature *459*, 379–385.

Pontes, B., Monzo, P., and Gauthier, N.C. (2017). Membrane tension: a challenging but universal physical parameter in cell biology. Semin. Cell Dev. Biol. *71*, 30–41.

Ramanujan, S., Pluen, A., McKee, T.D., Brown, E.B., Boucher, Y., and Jain, R.K. (2002). Diffusion and convection in collagen gels: implications for transport in the tumor interstitium. Biophys. J. *83*, 1650–1660.

Ranade, S.S., Syeda, R., and Patapoutian, A. (2015). Mechanically activated ion channels. Neuron *87*, 1162–1179.

Raucher, D., and Sheetz, M.P. (1999). Characteristics of a membrane reservoir buffering membrane tension. Biophys. J. *77*, 1992–2002.

Raucher, D., and Sheetz, M.P. (2000). Cell spreading and lamellipodial extension rate is regulated by membrane tension. J. Cell Biol. *148*, 127–136.

Rhee, J.M., Pirity, M.K., Lackan, C.S., Long, J.Z., Kondoh, G., Takeda, J., and Hadjantonakis, A.K. (2006). In vivo imaging and differential localization of lipid-modified GFP-variant fusions in embryonic stem cells and mice. Genesis *44*, 202–218.

Römer, W., Berland, L., Chambon, V., Gaus, K., Windschiegl, B., Tenza, D., Aly, M.R.E., Fraisier, V., Florent, J.C., Perrais, D., et al. (2007). Shiga toxin induces tubular membrane invaginations for its uptake into cells. Nature *450*, 670–675.

Rosholm, K.R., Leijnse, N., Mantsiou, A., Tkach, V., Pedersen, S.L., Wirth, V.F., Oddershede, L.B., Jensen, K.J., Martinez, K.L., Hatzakis, N.S., et al. (2017). Membrane curvature regulates ligand-specific membrane sorting of GPCRs in living cells. Nat. Chem. Biol. *13*, 724–729.

Sadegh, S., Higgins, J.L., Mannion, P.C., Tamkun, M.M., and Krapf, D. (2017). Plasma membrane is compartmentalized by a self-similar cortical actin meshwork. Phys. Rev. X *7*, 011031.

Saffman, P.G., and Delbrück, M. (1975). Brownian motion in biological membranes. Proc. Natl. Acad. Sci. USA *72*, 3111–3113.

Saha, S., Nagy, T.L., and Weiner, O.D. (2018). Joining forces: crosstalk between biochemical signalling and physical forces orchestrates cellular polarity and dynamics. Philos. Trans. R. Soc. Lond. B Biol. Sci. *373*, 20170145.

Saotome, K., Murthy, S.E., Kefauver, J.M., Whitwam, T., Patapoutian, A., and Ward, A.B. (2018). Structure of the mechanically activated ion channel Piezo1. Nature *554*, 481–486.

Schwarz, G., Callewaert, G., Droogmans, G., and Nilius, B. (1992). Shear stress-induced calcium transients in endothelial cells from human umbilical cord veins. J. Physiol. *458*, 527–538.

Schweitzer, Y., Lieber, A.D., Keren, K., and Kozlov, M.M. (2014). Theoretical analysis of membrane tension in moving cells. Biophys. J. *106*, 84–92.

Sens, P., and Plastino, J. (2015). Membrane tension and cytoskeleton organization in cell motility. J. Phys. Condens. Matter *27*, 273103.

Shaner, N.C., Lin, M.Z., McKeown, M.R., Steinbach, P.A., Hazelwood, K.L., Davidson, M.W., and Tsien, R.Y. (2008). Improving the photostability of bright monomeric orange and red fluorescent proteins. Nat. Methods *5*, 545–551.

Shen, H., Pirruccello, M., and De Camilli, P. (2012). SnapShot: membrane curvature sensors and generators. Cell *150*, 1300.e1–1300.e2.

Shi, Z., and Baumgart, T. (2015). Membrane tension and peripheral protein density mediate membrane shape transitions. Nat. Commun. *6*, 5974.

Shillcock, J.C., and Lipowsky, R. (2005). Tension-induced fusion of bilayer membranes and vesicles. Nat. Mater. *4*, 225–228.

Shin, W., Ge, L., Arpino, G., Villarreal, S.A., Hamid, E., Liu, H., Zhao, W.D., Wen, P.J., Chiang, H.C., and Wu, L.G. (2018). Visualization of membrane pore in live cells reveals a dynamic-pore theory governing fusion and endocytosis. Cell *173*, 934–945.e12.

St-Pierre, F., Marshall, J.D., Yang, Y., Gong, Y., Schnitzer, M.J., and Lin, M.Z. (2014). High-fidelity optical reporting of neuronal electrical activity with an ultrafast fluorescent voltage sensor. Nat. Neurosci. *17*, 884–889.

Singer, S.J., and Nicolson, G.L. (1972). The fluid mosaic model of the structure of cell membranes. Science *175*, 720–731.

Stewart, M.P., Helenius, J., Toyoda, Y., Ramanathan, S.P., Muller, D.J., and Hyman, A.A. (2011). Hydrostatic pressure and the actomyosin cortex drive mitotic cell rounding. Nature *469*, 226–230.

Thottacherry, J.J., Kosmalska, A.J., Elosegui-Artola, A., Pradhan, S., Sharma, S., Singh, P.P., Guadamillas, M.C., Chaudhary, N., Vishwakarma, R., and Trepat, X. (2017). Mechanochemical feedback and control of endocytosis and membrane tension. bioRxiv. https://doi.org/10.1101/201509.

Watanabe, S., Rost, B.R., Camacho-Pérez, M., Davis, M.W., Söhl-Kielczynski, B., Rosenmund, C., and Jorgensen, E.M. (2013). Ultrafast endocytosis at mouse hippocampal synapses. Nature *504*, 242–247.

Wen, P.J., Grenklo, S., Arpino, G., Tan, X., Liao, H.S., Heureaux, J., Peng, S.Y., Chiang, H.C., Hamid, E., Zhao, W.D., et al. (2016). Actin dynamics provides membrane tension to merge fusing vesicles into the plasma membrane. Nat. Commun. *7*, 12604.

Winkler, B., Aranson, I.S., and Ziebert, F. (2016). Membrane tension feedback on shape and motility of eukaryotic cells. Physica D *318*, 26–33.

Wu, M., Wu, X., and De Camilli, P. (2013). Calcium oscillations-coupled conversion of actin travelling waves to standing oscillations. Proc. Natl. Acad. Sci. USA *110*, 1339–1344.

Zakharova, O.M., Rosenkranz, A.A., and Sobolev, A.S. (1995). Modification of fluid lipid and mobile protein fractions of reticulocyte plasma membranes affects agonist-stimulated adenylate cyclase. Application of the percolation theory. Biochim. Biophys. Acta *1236*, 177–184.

Zeng, B., Chen, G.L., Garcia-Vaz, E., Bhandari, S., Daskoulidou, N., Berglund, L.M., Jiang, H., Hallett, T., Zhou, L.P., Huang, L., et al. (2017). ORAI channels are critical for receptor-mediated endocytosis of albumin. Nat. Commun. *8*, 1920.

STAR★METHODS

KEY RESOURCES TABLE

REAGENT or RESOURCE	SOURCE	IDENTIFIER
Chemicals, Peptides, and Recombinant Proteins		
1,2-dioleoyl-sn-glycero-3-phosphatidylcholine (DOPC)	Avanti Polar Lipids	cat# 850375
1,2-dioleoyl-sn-glycero-3-phosphatidylserine (DOPS)	Avanti Polar Lipids	cat# 840035
1,2-dioleoyl-sn-glycero-3-phosphoethanolamine (DOPE)	Avanti Polar Lipids	cat# 850725
1,2-distearoyl-sn-glycero-3-phosphoethanolamine-N-[biotinyl(polyethylene glycol)-2000] (DSPE-PEG(2000)-biotin)	Avanti Polar Lipids	cat# 880129
streptavidin coated beads	Polysciences, Inc	cat# 24158-1
Texas Red DHPE	Life Technologies	cat# T1395MP
pDisplayTM Mammalian Expression Vector	Thermo Fisher	cat# V66020
TransIT-X2	Mirus	cat# MIR6003
poly-d-lysine	Sigma	cat# P7205
matrigel	BD Biosciences	cat# 356234
complete mouse endothelial cell medium	Cell Biologics	cat# M1168
CellMask	Thermo Fisher	cat# C37608
Fluo-4-AM	Life Technologies	cat# F14201
Ionomycin	Thermo Fisher	cat# A20000
latrunculin B	Sigma	cat# 87612
glass capillaries	World Precision Instrument	cat# 1B150F-4
Anti-Digoxigenin coated polystyrene beads	Spherotech	cat# DIGP-40-2
$GdCl_3$	Sigma	cat# 203289-1G
GsMTx4	Tocris	cat# 4912
2-APB	Tocris	cat# 1224
Experimental Models: Cell Lines		
Henrietta Lacks (HeLa) cells	ATCC	CCL-2
Madin–Darby canine kidney (MDCK) epithelial cells	ATCC	CCL-34
NIH/3T3 fibroblasts	Zhuang Lab	N/A
Primary mouse brain endothelial (mBEC)	Rubin Lab	N/A
Primary rat hippocampal neurons	This work	N/A
Recombinant DNA		
pCAG: GPI-eGFP	Addgene, (Rhee et al., 2006)	32601
eGFP-KRAS or mOrange2-KRAS	This work	eGFP or mOrange2 targeted to the inner leaflet of plasma membrane using the C terminus sequence of KRAS
Lifeact-CFP	(Zeng et al., 2017)	gift
ASAP1	(St-Pierre et al., 2014)	gift
DRD2-eGFP	This work, Tian He	dopamine receptor D2 with eGFP
CheRiff-eGFP	(Hochbaum et al., 2014), Cohen Lab	N/A
eGFP-TM, or mOrange2-TM	This work	eGFP or mOrange2 targeted to the extracellular side of the plasma membrane, using a transmembrane helix from PDGF receptor on the pDisplay Mammalian Expression Vector
R-CaMP2	(Inoue et al., 2015)	gift

(*Continued on next page*)

Continued

REAGENT or RESOURCE	SOURCE	IDENTIFIER
GCaMP6f	Addgene (Chen et al., 2013)	40755
PIEZO1-mCherry	Ardem Patapoutian	gift
Software and Algorithms		
MATLAB R2015b	The Mathworks	https://www.mathworks.com/products/matlab.html
ImageJ	NIH	https://imagej.nih.gov/ij/
Other		
pipette puller	Sutter Instrument	P1000
microforge	World Precision Instrument	DMF1000
Sutter manipulators	Sutter Instrument	MP-285
digital micromirror device (DMD) with 608 × 684 pixels	Texas Instruments	LightCrafter

CONTACT FOR REAGENT AND RESOURCE SHARING

Further information and requests for resources and reagents should be directed to and will be fulfilled by the Lead Contact, Adam Cohen (cohen@chemistry.harvard.edu).

EXPERIMENTAL MODEL AND SUBJECT DETAILS

Cell culture, transfection, and staining

HeLa cells, NIH/3T3 fibroblasts, and MDCK cells were cultured following standard protocols. Briefly, cells were grown in DMEM supplemented with 10% FBS and penicillin/streptomycin in a 37°C incubator under 5% CO_2. Cells were grown to 50%–70% confluence in 3.5 cm dishes and transfected with 0.5 - 1 μg desired plasmid using TransIT-X2. One day after transfection, cells were trypsinized and re-plated at a density of 10,000 - 30,000 cells/cm^2 on glass-bottom dishes. Experiments were performed the following day. Before imaging, the cell culture medium was replaced with extracellular (XC) imaging buffer (125 mM NaCl, 2.5 mM KCl, 15 mM HEPES, 30 mM glucose, 1 mM $MgCl_2$, 3 mM $CaCl_2$, and pH 7.3).

All procedures involving animals were in accordance with the National Institutes of Health Guide for the care and use of laboratory animals and were approved by the Institutional Animal Care and Use Committee (IACUC) at Harvard. Hippocampal neurons from P0 rat pups were dissected and cultured in NBActiv4 medium at a density of 30,000 cells/cm^2 on glass-bottom dishes pre-coated with poly-d-lysine and Matrigel. At 1 day *in vitro* (DIV), glia cells were plated on top of the neurons at a density of 7000 cells/cm^2. At DIV5 - 7, neurons were transfected following the calcium phosphate protocol (Jiang and Chen, 2006). Imaging was performed 5 - 7 days after transfection, with neuron culture medium replaced with XC buffer.

Primary mouse brain endothelial cells were dissected and cultured in complete mouse endothelial cell medium. For tether imaging or Ca^{2+} imaging, cells were plated at a density of 10,000 - 30,000 cells/cm^2 on glass-bottom dishes and stained with CellMask for 10 min or with Fluo-4-AM for 30 min before experiments. For vesicle imaging, cells were grown to 50% confluence in 3.5 cm dishes and transfected with lenti-virus encoding mOrange2-TM. 5 - 7 days after transfection, cells were trypsinized and re-plated at a density of 10,000 - 30,000 cells/cm^2 on glass-bottom dishes. Experiments were performed 12 – 36 hr after cells were plated to glass-bottom dishes. Before imaging, the cell culture medium was replaced with XC buffer. Neurons and mBEC cells were fed twice weekly until experiments.

Sex information of cell lines and primary cultures is not available.

For nonspecific extracellular staining of transmembrane proteins, cells were incubated with 250 μg/mL Alexa Fluor 488 NHS Ester (dissolved using the original cell culture medium) for 30 min. Cells were then washed 3 - 5 times with 1 mL XC buffer before imaging. Amaranth, with a final concentration of 500 μM, was used to quench the Alexa488 fluorescence.

For imaging intracellular vesicles with FM4-64, cells were incubated with 20 μg/mL FM4-64 for 20 min. Cells were then washed 5 times with 1 mL XC buffer before imaging, leaving the cell with only intracellular vesicles stained. Fusion of vesicles was reported as the disappearance of fluorescent puncta (Gauthier et al., 2009). Ionomycin, with a final concentration of 5 μM, was used to trigger cell-wide vesicle fusion.

METHOD DETAILS

Bleb formation

Blebs were induced by treating the cells grown on glass bottom dish with 100 - 200 μM latrunculin B dissolved in 200 μL XC buffer. Blebs started forming within 3 min of drug addition. Then, 2 mL of XC buffer was added to the dish and majority of the blebs became stable for further experiments.

Please cite this article in press as: Shi et al., Cell Membranes Resist Flow, Cell (2018), https://doi.org/10.1016/j.cell.2018.09.054

Glass micropipette fabrication, tether pulling, and imaging

Micropipettes were pulled from glass capillaries using a pipette puller. The tip of the pipette was cut to an opening diameter of ~3 μm and bent to ~40° using a microforge. Experiments were performed on a home-built epi-fluorescence microscope (Kralj et al., 2011). Two Sutter manipulators controlled pipette motion.

The pipettes were immersed in a dispersion of 4 μm diameter Anti-Digoxigenin coated polystyrene beads, and suction was applied to plug each pipette aperture with a single bead. The beads were then brought into contact with cell membranes and retracted to pull out membrane tethers. A DMD with 608 × 684 pixels patterned the illumination to confine fluorescence excitation to the tether regions. In cases where tethers broke, the piece of tether attached to cells retracted to its mother cell within 1 min. To obtain large membrane tension changes on blebs through tether pulling, it is advantageous to choose more spherical blebs. Otherwise, on floppy blebs, a change of tether length for ~100 μm does not result in measurable changes in tether fluorescence (or equivalently, membrane tension).

Measurements of tension-dependent tether pulling force on GUVs (Figure S1) were performed on a home-built optical trap with 6 μm diameter streptavidin coated beads as described previously (Heinrich et al., 2010; Shi and Baumgart, 2015). Calibration between tether pulling force and tether intensity (with HeLa cells, as shown in Figures S2C and S2D) was achieved with simultaneous recording of pulling force (through the optical trap) and tether fluorescence (with patterned illumination).

Tether pulling and Ca^{2+} imaging

For simultaneous imaging of tethers and Ca^{2+} influx, MDCK cells were co-transfected with GPI-eGFP and R-CaMP2. Blue laser light (488 nm) for exciting GPI-eGFP was confined to the tether region via a digital micromirror device, while green laser light (532 nm) for exciting R-CaMP2 illuminated the whole cell (Figure 3B). Images were acquired continuously at 5 Hz with an emission filter simultaneously passing GFP and RFP emission wavelengths. Initiation points of Ca^{2+} influx were determined as the center of the Ca^{2+} influx (as shown in the heatmap of Figure 3C) in its first observable frame.

In the studies of the effects of Gd^{3+} and GsMTx4 (Figure 3D) on Ca^{2+} influx, MDCK cells were transfected with GCaMP6f as a Ca^{2+} reporter. Under wide-field 488 nm excitation, images were acquired continuously at 2 Hz with an emission filter for GFP.

In the study of the effect of PIEZO1 on Ca^{2+} influx, MDCK cells were co-transfected with PIEZO1-mCherry and GCaMP6f. PIEZO1-mCherry expressing cells were identified with 532 nm excitation and an emission filter for RFP. Images were acquired continuously at 2 Hz under wide-field 488 nm excitation with an emission filter for GFP.

All tether pulling experiments shown in Figures 3D and 3G followed the same tether pulling protocol (move the bead to gently touch a GCaMP6f expressing cell for 20 s, then pull bead away from the cell for 500 μm with the first 200 μm at 5 μm/s and the next 300 μm at 10 μm/s). Changes of GCaMP6f fluorescence (F_{max}/F_0) were measured in the region of bead-cell attachment (diameter 4 μm circle) with corrections for background and photo bleaching. F_{max} is the peak fluorescence during tether elongation; F_0 is the fluorescence baseline before tether pulling. We poked holes on the cells at the end of each tether pulling experiment to verify that the cells could report Ca^{2+} influx. In mBEC cells, the same tether pulling protocol was applied to cells stained with Fluo-4-AM (Figure 4A).

Tether pulling and vesicle fusion

The same tether pulling protocol used for MSC activation and Ca^{2+} imaging was applied to cells expressing mOrange2-TM (Figures 3G and 4B). Under wide-field 532 nm excitation, images were acquired continuously at 1 Hz with a 562/40 nm bandpass filter. Vesicle fusion sites were determined as the center of bright dots that appeared during pulling (as shown in the heatmap of Figures 3G and 4B).

To determine the distribution of tether-vesicle distances expected from the null hypothesis (vesicles fuse at random locations in the cell), the image of each cell was converted into a binary mask. The mean distance from the tether location to all points on the cell was then calculated. This distance was averaged over all cells measured.

In the study of the effect of 2-APB (Figure 4D) on vesicle fusion in mBEC cells, mOrange2-TM transfected cells were incubated with 100 μM 2-APB in cell culture medium for 1 hr to deplete ER Ca^{2+} stores. The medium was then replaced with XC buffer for imaging.

Local flow experiments with mBEC cells

mBEC cells were stained with Fluo-4-AM or transfected with mOrange2-TM as described above. Pipettes with an exit diameter of $R_p = 12$ μm were used to inject XC buffer near one end of the cell by quickly increasing the pressure inside pipette. Fluorescence images were acquired at 2 Hz. The flow speed was calibrated by measuring the rate of decrease of buffer volume in the pipette. For data shown in the main text, this rate was $G = 14$ nL/s. Buffer speed exiting pipette was calculated by $v_{flow} = G/(\pi R_p^2) = 12$ cm/s. Maximal surface shear induced by the pipette was approximately $v_{flow}/R_p = 2 \times 10^4\ s^{-1}$, corresponding to a surface stress of $\eta_c \cdot v_{flow}/R_p = 20\ pN/\mu m^2$. Here, $\eta_c = 10^{-3}\ Pa \cdot s$ is the viscosity of XC buffer.

All experiments with cells were performed with a 60x oil objective (Olympus UIS 2, N.A. 1.49) with an objective heater (Bioptechs) to keep the sample at 37°C.

Please cite this article in press as: Shi et al., Cell Membranes Resist Flow, Cell (2018), https://doi.org/10.1016/j.cell.2018.09.054

QUANTIFICATION AND STATISTICAL ANALYSIS

Tether imaging analysis

Tether diameters were estimated by imaging HeLa cells expressing membrane-bound fluorescent proteins. By measuring the cumulative fluorescence I_{cell} in a patch of flat cell membrane of area A_{cell} and the cumulative fluorescence I_{tether} on tethers (pulled from the same cell) of length l (Figure S2B), the diameter of a single tether is calculated using:

$$d_{tether}=\frac{2I_{tether}A_{cell}}{\pi I_{cell}l}.$$

The factor of 2 in the numerator accounts for the fact that the cell has top and bottom membranes, both of which contribute to I_{cell}.

Fluorescence recovery after photobleaching (FRAP) measurements of diffusion

To measure tracer diffusion on cell membranes, a flat patch of membrane was photobleached within a circular region of radius $r = 7\ \mu\text{m}$ at an illumination intensity of 1 kW/cm^2 for ~60 s. Then an illumination intensity of 0.5 W/cm^2 was used to monitor the recovery. To measure tracer diffusion on tethers, the same laser spot was used to bleach a $d = 14\ \mu\text{m}$ long region of tether. Measurements on plasma membrane and tether were performed sequentially on the same cells.

For FRAP measurements on the cell, the fluorescence recover was fit to the relation:

$$I(t)=\frac{I_0+I_\infty\dfrac{t}{\tau_{0.5}}}{1+\dfrac{t}{\tau_{0.5}}}.$$

The diffusion coefficient was extracted using (Kang et al., 2012) $D_s^{cell} = r^2/4\tau_{0.5}$.

For FRAP measurements on the tether, the recovery phase was fit to:

$$I(t)=I_\infty-I_0\exp(-t/\tau_{exp}).$$

The diffusion coefficient was extracted using (Rosholm et al., 2017) $D_s^{tether} = 4d^2/\pi^2\tau_{exp}$. The high membrane curvature in tethers is reported to slightly decrease diffusion relative to a planar bilayer (by less than a factor of 2) (Domanov et al., 2011), an effect that we neglected.

FRAP measurement of fraction of transmembrane proteins that are immobile

To measure the immobile fraction of cell surface proteins, NHS-ester Alexa 488 labeled cells were bleached with a donut shape laser beam (inner radius 17.5 μm, outer radius 35 μm) following the procedure described above.

The immobile fraction of proteins was calculated using

$$\frac{\phi_i}{\phi_t}=\frac{I_{center}^{end}-I_{ring}^{end}}{I_{center}^{0}-I_{ring}^{0}}.$$

Here, the ϕ_t represents the area fraction of all labeled transmembrane proteins. I_{center}^0 and I_{ring}^0 represent fluorescence intensities right after photobleaching in unbleached and bleached regions respectively (at t ~100 s, see Figure 2E). I_{center}^{end} and I_{ring}^{end} represent fluorescence intensities, in unbleached and bleached regions respectively, at the end of the FRAP experiment (t = 1000 s).

Simulation of relaxation of membrane tension in a tether

To model tension relaxation in a pulled tether, we decomposed the experiment into three steps:

(I) Initial equilibrium

Tether length l, radius r and membrane tension, σ, are related by:

$$A=2\pi rl,$$

$$\sigma=\frac{\kappa}{2r^2}.$$

Here, A is the tether surface area; κ is the bending stiffness of the membrane.

Combining these two relations leads to an expression for membrane tension as a function of tether length and area:

$$\sigma(A,l)=\frac{2\pi^2\kappa l^2}{A^2}.$$

(II) Elongation of tether at constant velocity, v_{pull}

The simulation is broken into small time-steps of length $\Delta t = 3$ s. For each time-step, the dynamics are described by three processes:

1: At constant tether area, A, increase tether length by $\Delta l = v_{pull}\Delta t$. Then update l, r, and σ, without allowing flow of lipids from the cell into the tether:

$$l \rightarrow l + \Delta l,$$

$$r = \frac{A}{2\pi l},$$

$$\sigma \rightarrow \sigma + \frac{4\pi^2\kappa}{A^2} l \Delta l.$$

2: Calculate the diffusion of tension in the cell membrane, treating the membrane as a 20 μm radius disk and matching tension across the cell-tether boundary at radius r:

$$\frac{\partial\sigma}{\partial t} = D_\sigma \nabla^2 \sigma.$$

3: Calculate flow of lipids from the cell membrane into the tether, keeping l constant. The flux into the tether is given by the solution to the tension diffusion equation at the cell-tether boundary:

$$\Delta A = 2\pi r \frac{k\nabla\sigma}{\eta}\Delta t$$

$$A \rightarrow A + \Delta A,$$

$$\sigma \rightarrow \sigma - \frac{4\pi^2\kappa l^2}{A^3}\Delta A.$$

(III) Relaxation of tension via lipid flow into a tether of constant length

The steps are the same as in (II) except that tether length is always kept constant. The results of these simulations are plotted in Figure 2F.

Relation between tether radius, pulling force, and membrane tension

For a tube of length l and radius r, the free energy of a tether U is (Brochard-Wyart et al., 2006; Derényi et al., 2002):

$$U = 2\pi r l\left(\frac{\kappa}{2r^2} + \sigma\right) - fl \tag{S1}$$

Here κ is the bending stiffness of the membrane, σ is membrane tension, and f is the external pulling force.

The surface tension acts to reduce the radius (and therefore decrease the total area of the tether) while the bending stiffness works to increase the radius (to avoid membrane bending). The balance between these two forces sets the mechanical equilibrium. The equilibrium radius r_0 and pulling force f_0 are obtained from:

$$\frac{\partial U}{\partial r} = 2\pi l\left(-\frac{\kappa}{2r^2} + \sigma\right) = 0$$

and

$$\frac{\partial U}{\partial l} = 2\pi r\left(\frac{\kappa}{2r^2} + \sigma\right) - f = 0$$

from which we obtain:

$$r_0 = \sqrt{\frac{\kappa}{2\sigma}} \tag{S2}$$

and

$$f_0 = 2\pi\sqrt{2\kappa\sigma} \tag{S3}$$

These equations show that one can determine the tension of a bilayer by measuring either the tether radius or the pulling force.

Hydrodynamics of lipid flow

To describe lipid flow through a medium comprised of randomly dispersed immobile obstacles, the Stokes equation is augmented with a drag term (Bussell et al., 1995; Howells, 1974) $(\eta/k)\vec{v}$:

$$\nabla\sigma = -\eta\nabla^2\vec{v} + \frac{\eta}{k}\vec{v} \tag{S4}$$

where σ is the membrane tension, η is the two-dimensional membrane viscosity, $\vec{v}$ is the velocity field of lipid flow, and k is the Darcy permeability of the array of obstacles. When the Brinkman equation is written for pressure, rather than membrane tension, the signs on the right-hand side are reversed (fluids flow from high to low pressure, but membranes flow from low to high tension). Physically, the ratio η/k is the drag coefficient of a fixed array of obstacles.

Conservation of mass requires that:

$$\frac{\partial\rho}{\partial t} + \nabla\cdot(\rho\vec{v}) = 0 \tag{S5}$$

where ρ is the two-dimensional density of lipids. Assuming a small perturbation to lipid density, $\rho = \rho_o + \delta\rho$, Eq. S5 becomes:

$$\frac{\partial\rho}{\partial t} = -\rho_o\nabla\cdot\vec{v} \tag{S6}$$

We assume a linear stress-strain relation for the membrane tension (Hochmuth et al., 1973):

$$\delta\sigma = -E_m\,\delta\rho/\rho_o \tag{S7}$$

where E_m is the effective area expansion modulus of the cell membrane. Equations S4, S6, and S7 describe the hydrodynamics of lipid flow in cell membranes containing random arrays of fixed obstacles. The equations can be combined to obtain:

$$\frac{E_m}{\eta}\nabla^2\sigma = \left(-\nabla^2 + \frac{1}{k}\right)\frac{\partial\sigma}{\partial t} \tag{S8}$$

Neglect of membrane obstacles is equivalent to keeping only the first term on the right-hand side of Eq. S4 or S8.

$$\frac{\partial\nabla^2\sigma}{\partial t} = -\frac{E_m}{\eta}\nabla^2\sigma \tag{S9}$$

This relation identifies a relaxation time for tension fluctuations, $\tau = \eta/E_m$. Inserting estimates of membrane viscosity ($\eta = (3.0 \pm 0.4) \times 10^{-3}$ pN•s/μm) and area expansion modulus ($E_m = 40$ pN/μm)(Hochmuth, 2000) gives a relaxation time less than 0.1 ms, as has been used in the literature (Keren et al., 2008).

If the spacing between transmembrane obstacles is small compared to externally imposed variations in the flow field, then the second term of Eq. S4 or S8 dominates, and we obtain a diffusion-like equation for membrane tension:

$$\frac{\partial\sigma}{\partial t} = D_\sigma\nabla^2\sigma \tag{S10}$$

with

$$D_\sigma = \frac{E_m k}{\eta}. \tag{S11}$$

In other words, if l_c is a characteristic length scale of variations in σ then Eq. S10 applies when $(k/l_c^2) \ll 1$. The same result describes the three-dimensional propagation of pressure in a porous elastic medium (Charras et al., 2005).

Please cite this article in press as: Shi et al., Cell Membranes Resist Flow, Cell (2018), https://doi.org/10.1016/j.cell.2018.09.054

Calculation of drag due to a random array of fixed cylinders

When N_i immobile proteins are present in a piece of membrane with area A, the immobile area fraction is $\phi_i = N_i \pi a^2 / A$, where a is the radius of one immobile particle. Bussel et al.(Bussell et al., 1995) adapted Howell's mean-field solution of the Stokes equation for a random array of cylindrical obstacles (Howells, 1974) to calculate the mean force, $\vec{F}_0$, required to drag one particle with a mean velocity $\vec{U}$ through the background of immobile particles.

We introduce the dimensionless quantity $x = a/k^{1/2}$, where a is the radius of an obstacle and k is the Darcy permeability coefficient. Then:

$$\vec{F}_0 = \frac{\vec{U}}{m_b} = 4\pi\eta \left(\frac{x^2}{2} + \frac{xK_1(x)}{K_0(x)} \right) \vec{U} \tag{S12}$$

Here, m_b is the mobility of the tracer particle, and K_0 and K_1 are the modified Bessel functions of the second kind with orders of 0 and 1, respectively.

According to the Brinkmann model, the mean force per unit area to drag the membrane at velocity $\vec{U}$ is:

$$\frac{\phi_i}{\pi a^2} \vec{F}_0 = \frac{\eta}{k} \vec{U} \tag{S13}$$

Together, these two equations lead to the relation between permeability and immobile protein fraction:

$$\phi_i = \frac{x}{2x + 4\frac{K_1(x)}{K_0(x)}} \tag{S14}$$

The dimensionless diffusion coefficient of tracer molecules is related to the mobility via:

$$\frac{\pi\eta D_s}{k_B T} = \pi\eta m_b = \frac{1}{2x^2 + 4x\frac{K_1(x)}{K_0(x)}} \tag{S15}$$

The dimensionless diffusion coefficient of membrane tension is:

$$\frac{\eta D_\sigma}{E_m a^2} = \frac{k}{a^2} = \frac{1}{x^2} \tag{S16}$$

The upper limit of tracer diffusion is given by the Saffman–Delbrück model (Saffman and Delbrück, 1975):

$$\frac{\pi\eta D_s^{max}}{k_B T} = \frac{1}{4}\left[\ln\left(\frac{\eta}{\eta_c a} \right) - 0.577 \right] \tag{S17}$$

where η_c is the viscosity of the fluid medium surrounding the membrane and it is assumed that $(\eta/\eta_c a) \gg 1$.

For diffusion of tension, hydrodynamic coupling to the cytoskeleton exerts viscous drag even in the absence of fixed obstacles. This drag sets an upper bound on the diffusion coefficient for membrane tension:

$$\frac{\eta D_\sigma^{max}}{E_m a^2} = \frac{\eta h}{\eta_c a^2} \tag{S18}$$

where h is the distance between the cortical cytoskeleton and the plasma membrane (see Figure 2). We used $\eta_c = 10^{-3}$ pN$\cdot$s/μm^2, a = 2 nm (Bussell et al., 1995), and h = 20 nm (Clausen et al., 2017).

Equation of state of membranes

The relation between the projected membrane density and the membrane tension is given in equation [S7]. The resting tension of the cell membrane (~25 pN/µm) is much lower than the tension where enthalpic stretching of lipid bilayers becomes significant (500 pN/µm) (Evans and Rawicz, 1990). Microscopically, the membrane has undulations due to thermal fluctuations, due to fluctuations in the underlying cytoskeletal support, and possibly due to binding of curvature-inducing proteins (Shen et al., 2012) (e.g., in caveolae). The membrane density, ρ_0, refers to a projected density of lipids after averaging over these microscopic undulations. Tension can partially smooth these undulations, leading to an effective stretching modulus that does not involve changing the mean spacing between lipid molecules. Experimental measurements of the effective area expansion modulus of cells (Hochmuth, 2000) indicate that the apparent elasticity is mainly associated with structures such caveolae and microvilli and the contribution from thermal agitation is negligible (Evans and Rawicz, 1990; Hochmuth et al., 1973; Hochmuth, 2000).

Supplemental Figures

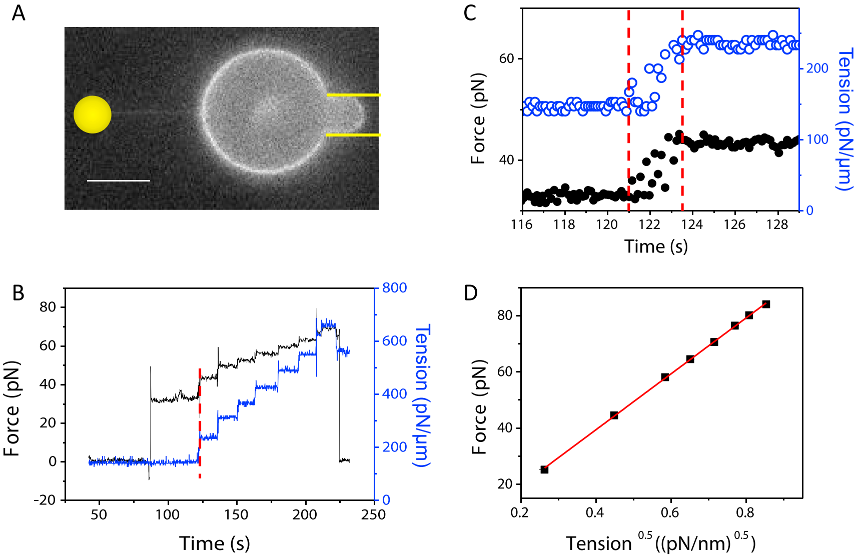

Figure S1. Membrane Tension Equilibrates Quickly in Artificial Lipid Bilayers, Related to Figure 1

(A) Fluorescence image of a micropipette-aspirated GUV (DOPS:DOPE:DOPC = 35:30:35) containing 0.5% DSPE-Bio-PEG2000 and labeled with 0.3% Texas Red DHPE. The edge of the pipette is marked with yellow lines. An optically trapped bead (position indicated by the yellow circle) pulled a membrane tether opposite to the pipette. Scale bar 10 μm.

(B) Changes in membrane tension (blue) were induced by applying steps of pressure to the pipette and tether pulling force (black) was monitored via the optical trap.

(C) Close-up of the step marked with a red line in (B), showing no detectable delay between change in tension and change in tether force. Measurements sampled at 10 Hz.

(D) Relation between tether pulling force and the square root of membrane tension, with a linear fit following the relation: $f = 2\pi\sqrt{2\kappa\sigma}$ (red line, $R^2 = 0.99$). Error bars are SEM.

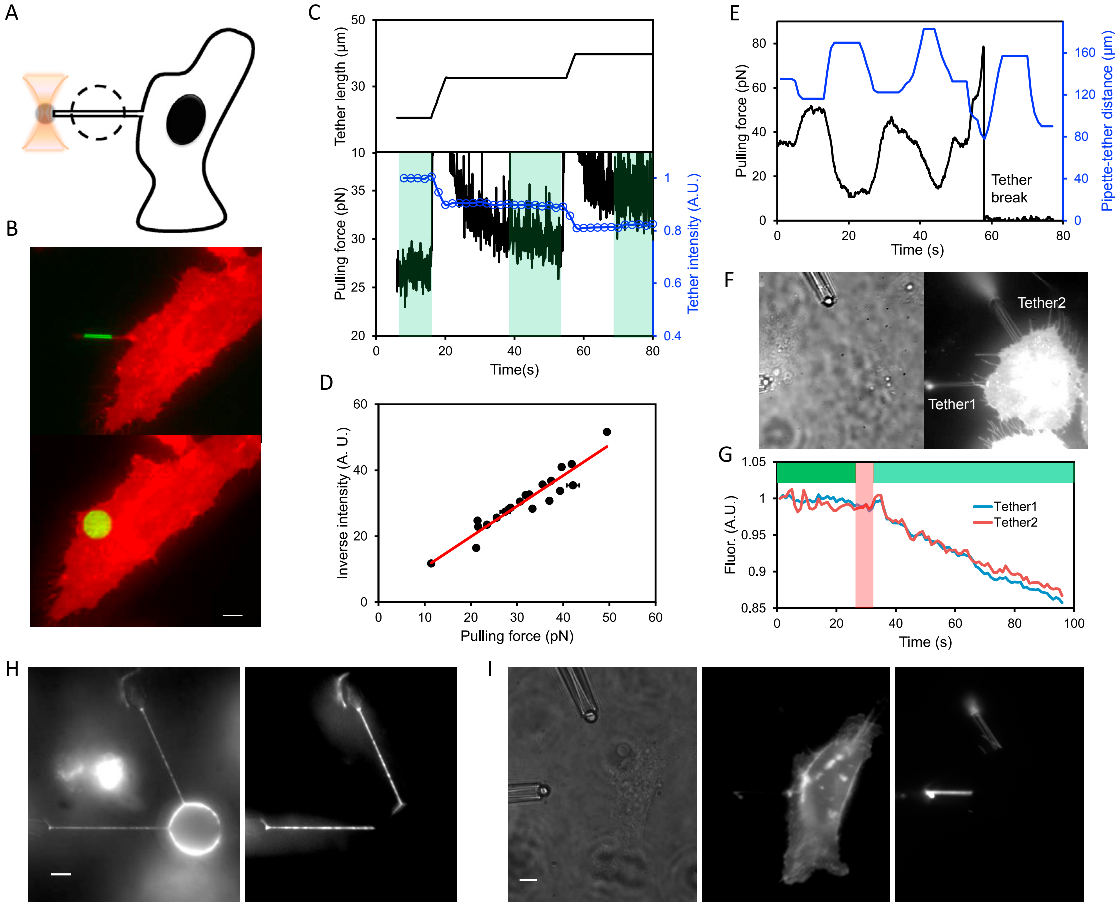

Figure S2. Tether Diameter Reports Membrane Tension, Related to Figure 1

(A) Schematic showing simultaneous measurement of tether pulling force (with an optical trap) and tether fluorescence intensity (with patterned illumination in the dashed circle).

(B) Determination of tether diameter from tether fluorescence intensity. A 14 μm diameter circular spot of illumination was first directed to a tether (top) and then to a flat portion of the parent cell (bottom). The ratio of the total fluorescence excited in these two configurations equals the ratio of illuminated membrane areas. These calibrations yielded an average tether diameter d_{tether} = 150 ± 10 nm (mean ± SEM, n = 5 cells) for tethers ~20 μm long. Measured average tether pulling force was f_{tether} = 16 ± 1 pN (mean ± SEM, n = 10 cells), leading to a membrane bending stiffness $\kappa = (1.9 \pm 0.2) \times 10^{-19}$ J. Scale bar, 10 μm.

(C) Tethers were pulled with a bead in an optical trap, and tether length, fluorescence intensity, and force were measured simultaneously. Regions shaded in green were used to calculate the relation between steady state tether fluorescence intensity and pulling force.

(D) Relation between tether pulling force and inverse of tether fluorescence intensity (normalized to expression level; R^2 = 0.9, n = 7 cells). Error bars are SEM.

(E) Perturbation to membrane tension via osmotic shocks. Tether pulling force was measured with an optical trap while a pipette flowed pure water over the cell. As the pipette approached the cell, the pulling force increased, signaling an increase in membrane tension. As the pipette withdrew, the tension decreased.

(F) Transmitted light (left) and fluorescence (right) images showing two sets of tethers pulled from the same cell.

(G) Response of tether fluorescence to gradual addition of hypotonic buffer (20 mOsm buffer added to equal volume of 300 mOsm XC buffer during time shaded in red). Experiments were performed at 37°C on HeLa cells expressing membrane-targeted fluorescent protein mOrange2-KRAS (A) – (E) and GPI-eGFP (F), (G).

(H) Left: Wide-field epifluorescence image of a bleb in a HeLa cell expressing GPI-eGFP with two tethers. Right: Same structure, with patterned illumination restricted to illuminating the tethers. (I) Left: Transmitted light image of two pipettes with polystyrene beads at the ends. Middle: Wide-field epifluorescence image of a HeLa cell expressing GPI-eGFP. Right: Same structure, with patterned illumination restricted to illuminating the tethers.

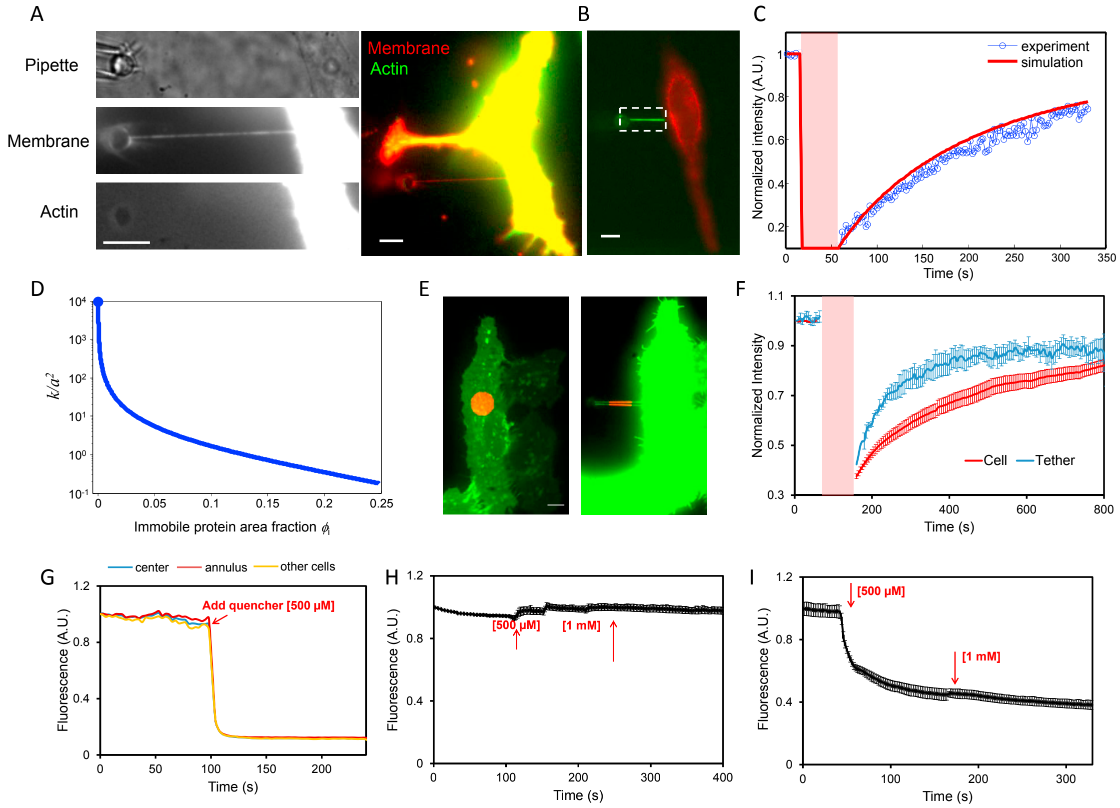

Figure S3. FRAP Measurements of Molecular Transport in Cell Membranes, Related to Figure 2

(A) Actin cytoskeleton does not penetrate membrane tethers. Top left: transmitted light image showing position of the tether pulling pipette. Middle and bottom left: Simultaneous images of cell membrane (mOrange2-KRAS) and actin (Lifeact-CFP) in a tether. Images were taken 15 min after tether formation. Right: Composite image of the whole cell. Red: membrane, green: actin.

(B) FRAP experiment to test whether tether and cell membrane are in diffusive equilibrium. Composite fluorescence image showing the photobleached region (dashed box) on a tether (green), attached to a HeLa cell (red) expressing DRD2-eGFP.

(C) FRAP of the tether (blue) and corresponding simulation (red) assuming free diffusion from cell to tether. The simulation used the experimentally measured diffusion coefficient of DRD2-eGFP on the cell, $D_{\mathrm{s}}(\mathrm{Cell}) = 0.037\ \mu\mathrm{m}^2/\mathrm{s}$ (see Table S2), and a tether radius of 75 nm. Since $D_{\mathrm{s}}(\mathrm{Cell}) << D_{\mathrm{s}}(\mathrm{Tether})$, the smaller diffusion coefficient dominated the transport and was the appropriate choice for the simulations. The simulation was performed in MATLAB. Time of photobleaching is shaded red.

(D) Relation between Darcy permeability k and area fraction of immobile proteins ϕ_i. The function $k/a^2 = f(\phi_i)$ was derived by Bussell (Bussell et al., 1995) et al., who showed that $\varphi_i = x/[2x + 4(K_1(x)/K_0(x))]$, where $x = a/k^{1/2}$ (see Quantification and Statistical Analysis). The upper limit (blue dot) is calculated from viscous drag of the cytoplasm layer between membrane and actomyosin cortex.

(E) Composite images showing the cell (green) and 14 μm circular photobleaching spot (red). Left: FRAP on cell membrane. Right: FRAP on tether.

(F) FRAP data in HeLa cells expressing DRD2-eGFP. Error bars represent SEM from n = 10 tethers pulled from 10 cells. Time of photobleaching is shaded red.

(G) After the FRAP measurement as shown in Figure 2E, a cell impermeant fluorescent quencher, amaranth, was added to a final concentration of 500 μM to quench the Alexa488 fluorescence. Fluorescence of all regions of the cell membrane dropped to background levels, establishing that there was no detectable internalization of fluorescently labeled proteins.

(H and I) Validation that amaranth functions as a cell-impermeant fluorescence quencher. (H) In cells expressing intracellular eGFP (eGFP-KRAS) amaranth did not affect fluorescence, but (I) in cells expressing extracellular eGFP (pDisplay: eGFP-TM) amaranth quenched fluorescence. Error bars are SEM over n = 4 cells for eGFP-KRAS and n = 5 cells for eGFP-TM. Scale bars in all panels 10 μm.

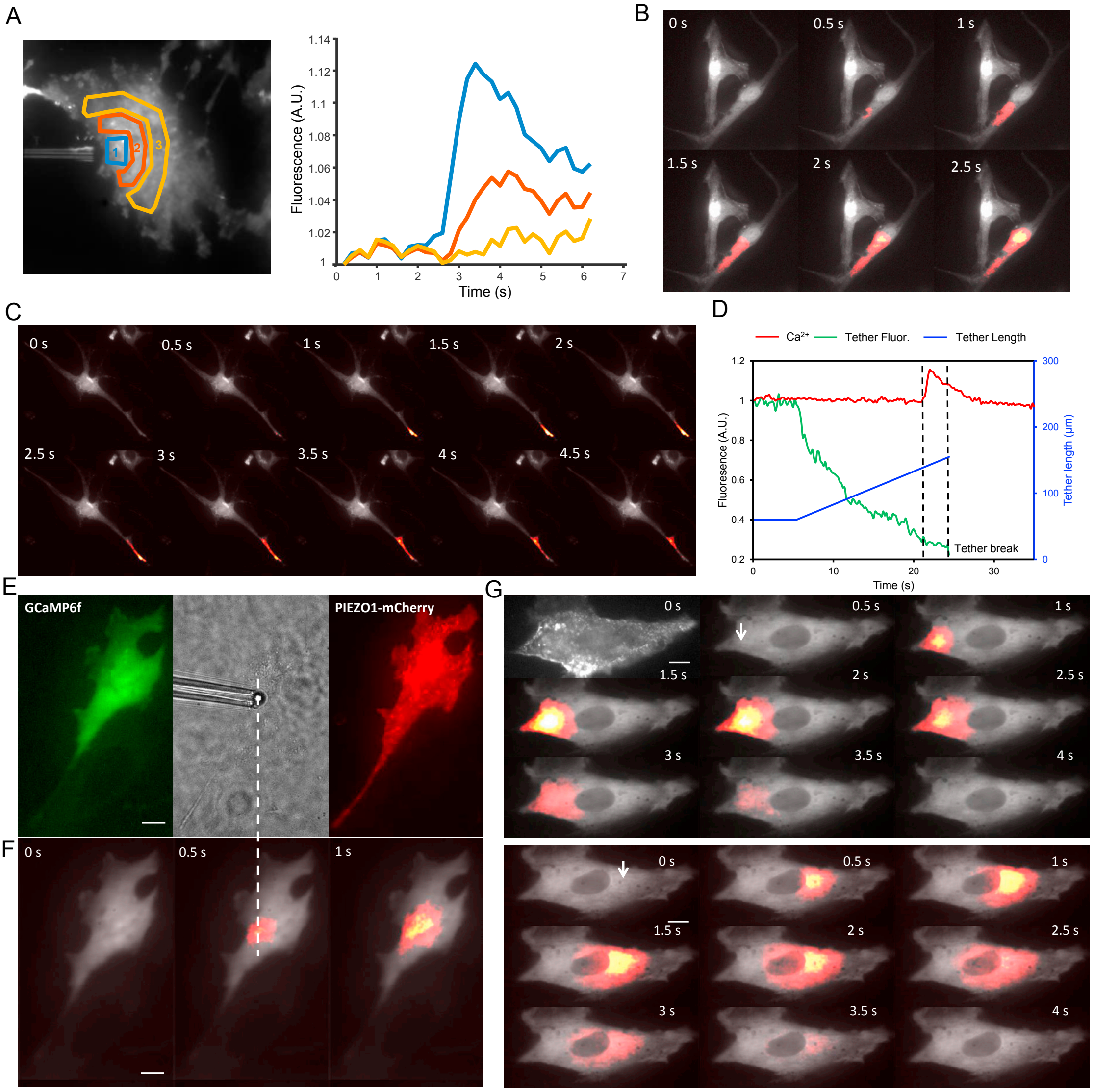

Figure S4. Dynamics of Ca^{2+} Entry through Mechanosensitive Ion Channels, Related to Figures 3 and 4

(A) MDCK cell from Figure 3C. Fluorescence of the R-CaMP2 reporter in different regions of interest as a function of time after initial Ca^{2+} influx. The dynamics show diffusion of Ca^{2+} from the point of tether attachment into the cell.

(B) mBEC cell from Figure 4A. Filmstrip of fluorescence recordings in response to activation of mechanosensitive ion channels via tether pull. The movie shows local activation followed by intracellular spread of Ca^{2+}.

(C) mBEC cell of Figure 4E. Filmstrip of fluorescence recordings in response to local shear flow. The Ca^{2+} influx starts at the region of maximum shear, followed by intracellular propagation of Ca^{2+}.

(D) In experiments as shown in Figure 3B, tether fluorescence intensity reports tether radius. Membrane tension can then be estimated from $\sigma = \kappa / 2r_0^2$ (see Quantification and Statistical Analysis). The activation tension of MSCs was found to be approximately 11 times higher than the resting tension of the cell (dashed line, resting membrane tension is ~25 pN/µm). This estimate of activation tension is a lower bound because at the time of MSC activation the tether was still elongating, so tether diameter was not fully equilibrated.

(E) MDCK cell co-expressing GCaMP6f (green) and PIEZO1-mCherry (red), with a pipette-controlled bead locally touching the cell (gray).

(F) Localized Ca^{2+} influx triggered by tether stretch. Dashed line shows the tether attachment point. Ca^{2+} diffused from the point of entry to gradually fill the cell. There was no evidence of Ca^{2+} entry at any point other than the site of tether attachment.

(G) Sequential tether pulling from two points on the same cell (white arrows). Top: pulling from left edge of the cell. The image at t = 0 shows the expression of PIEZO1-mCherry. Bottom: pulling from the right sides of the same cell. For both tether pulls, Ca^{2+} diffused from the point of entry to gradually fill the cell. There was no evidence of Ca^{2+} entry at any point other than the site of tether attachment. Images in B, C, F and (G) are composites of mean fluorescence (gray) and changes in fluorescence (heatmap). Scale bars in all panels 10 µm.

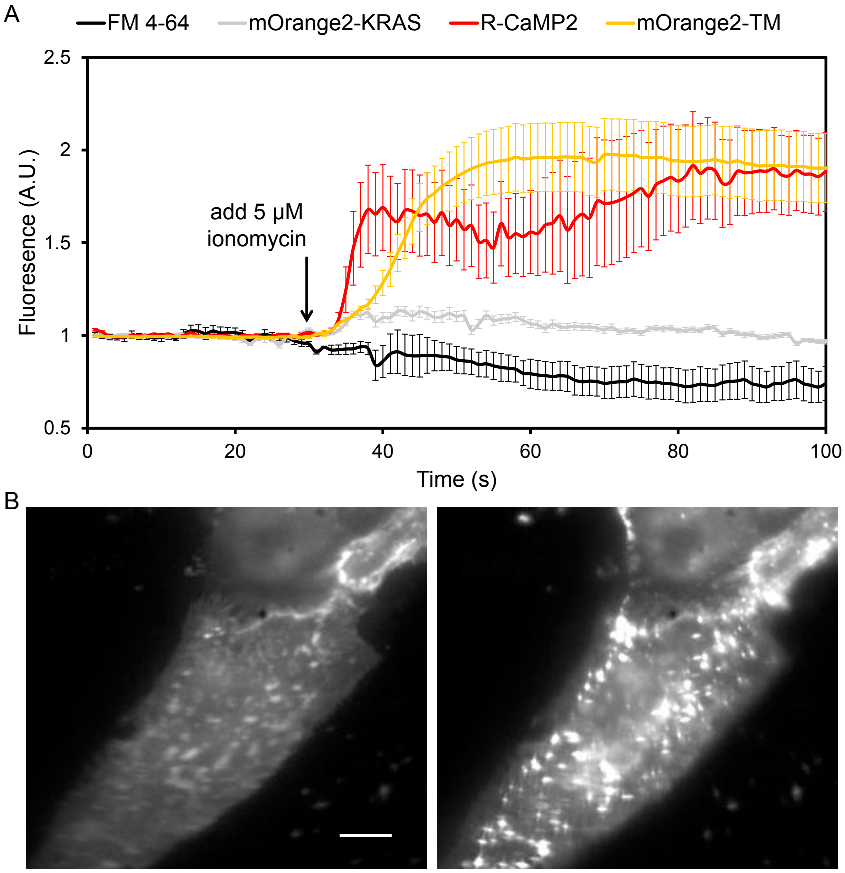

Figure S5. Validating mOrange2-TM as a Vesicle Fusion Reporter, Related to Figure 3

(A) Validating ionomycin as a means to induce vesicle fusion. In MDCK cells expressing R-CaMP2, ionomycin (5 μM) induced a rapid increase in fluorescence (red, n = 4 cells) indicating Ca^{2+} influx. Fresh MDCK cells were incubated with FM4-64 to load the dye into vesicles and then the dye was washed from the extracellular medium. Ionomycin led to a decrease in fluorescence (black, n = 4 cells), consistent with ionomycin-induced vesicle fusion. In MDCK cells expressing mOrange2-TM, ionomycin induced a rapid increase in fluorescence (orange, n = 7 cells), consistent with vesicle fusion and de-acidification of the vesicles. As a control experiment, ionomycin was added to MDCK cells expressing mOrange2-KRAS, which targeted the fluorescent protein to the inner leaflet of plasma membrane and to the cytoplasmic surface of vesicles. Ionomycin did not affect the fluorescence of these cells (gray, n = 5 cells). Error bars are SEM.

(B) Image of MDCK cells expressing mOrange2-TM before (left) and after (right) adding ionomycin. Scale bar 10 μm.

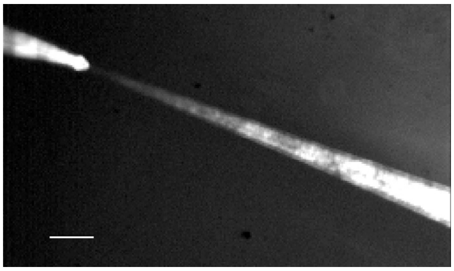

Figure S6. Tracking the Flow Profile from the Pipette for Shear Perturbation to Cells, Related to Figure 4

The pipette is on the upper left. The flow was visualized with fluorescent beads. Scale bar 100 μm.